I4P : an Igor Pro suite for photoemission analysis

Rémi Lazzari

I4P : an *Igor Pro* suite for photoemission analysis

Rémi Lazzari[a,b,*]

[a] *CNRS, Sorbonne Université, UMR 7588, Institut des NanoSciences de Paris (INSP), F-75005 Paris, France*
[b] *Fédération de Recherche Spectroscopies de Photoémission, CNRS FR 2050*

Abstract

A package based on the *Igor Pro* scripting language is proposed for the analysis of photoemission spectroscopy data (XPS, HAXPES, UPS). Compared to the already numerous available softwares, the *Igor Pro Paris Photoemission Package (I4P)* gathers in a single tool: (i) basic data analysis and plotting features (such as satellite/ghost line deconvolution, inelastic background subtraction, determination of the intensity-energy response function and its correction, peak overlap, energy-mass conversion in ion scattering spectroscopy), (ii) databases of binding energies, of photo-ionization cross sections, of (in)elastic mean free paths and effective attenuation lengths, (iii) quantification based on elastic peak areas accounting for elastic scattering, (iv) depth profiling by angle-resolved photoemission and by inelastic background analysis, (iv) peak fitting with 17 different line shapes including background and fully configurable constraints between fit parameters. Aside a detailed manual including the references to the relevant literature, *I4P* comes not only with a graphical interface but also with scripting commands. Most of all, the free availability of the source code allows the potential user to easily develop additional options of data treatment.

Keywords: x-ray and uv photoemission, peak fitting, quantification, databases, software

1. Introduction

Photoemission spectroscopy, under x-ray (XPS) or ultra-violet (UPS) excitations, is a major and well-established tool in material science [1–3]. Its popularity is related to the capabilities of the technique to identify elements via their core level fingerprints, to probe their chemical environment via binding energy shifts and to quantify sample composition. Beyond the increasing need of interface and nanostructure characterisation, its widespread use is also due to the easy access to stand-alone laboratory spectrometers and to advanced synchrotron-based set-ups. The technique benefits from continuous instrumental developments allowing nowadays near-ambient condition photoemission, *operando* measurement on devices, hard x-ray photoemission spectroscopy (HAXPES) with an increased in-depth sensitivity, to cite only a few. The theoretical foundations of this spectroscopy have been continuously improved over the years, in particular regarding the description of (i) inelastic losses [4, 5], (ii) inelastic mean free paths [6], (iii) elastic electron transport and effective attenuation lenghts [7–11], (iv) photo-ionisation cross sections [12, 13], (v) line shape description and quantification [5, 14]. Due to its intrinsic surface sensitivity and the complex mixtures of initial/final states and satellites in peak profiles, not speaking about experimental errors (sample mounting [15], charge effects and their compensation [16], calibration and referencing [16, 17], transmission function [18], etc...), photoemission analysis requires trained users and efficient softwares to avoid flaws in the data interpretation and erroneous conclusions [19]. Beyond the general advise of a careful comparison to existing literature [20], best practices [21–24] have been established concerning data acquisition, inelastic background handling, peak fitting and quantification. Thus all the concepts behind photoemission analysis have been progressively implemented in a great wealth of softwares (see web sites [25, 26]). To cite a few, *CasaXPS* [27] and *UniFit* [28] are well-established tools for peak fitting and quantification. The suite *QUASES* [29] allows for depth-profiling of nanostructured materials by angle-resolved photoemission or inelastic background analysis. Somehow similar analysis can be performed with the *SESSA* program [30, 31] with Monte-Carlo simulations. Inelastic mean free paths and effective attenuation lengths can be obtained using dedicated softwares from tabulated dielectric calculations or effective formulas [30, 32, 33]. Several compilations of the photo-ionisation cross sections can be found in the literature [12, 13, 34–36] but, most of the time, only the Scofield one is used and non-dipolar terms relevant in HAXPES cannot be easily included. Databases of relative sensitivity factors are often provided by instrument suppliers but cannot be transferred to other set-ups or used for structured materials. Indeed, they intrinsically include contributions from apparatus transmission function and from the energy dependence of

*Corresponding author
Email address: remi.lazzari@insp.jussieu.fr (Rémi Lazzari)

inelastic mean free paths and are valid, in principle, only for homogeneous materials.

In fact, most existing photoemission analysis tools are either proprietary (*i.e.* linked to a machine supplier such as *Avantage* by *ThermoFisher Scientific*, *MultiPak* by *PhysicalElectronics*), or not fully free-of-charge, or not easily modifiable by the potential user, or not fully documented or up-to-date in terms of databases, or with restricted fitting options, or dedicated to only one aspect of the analysis. This paper describes a suite, called *Igor Pro Paris Photoemission Package (I4P)* [37], for the treatment of photoemission in every sense. Written under the *Igor Pro* [38] scripting language, *I4P* gathers, in a single tool, basic data treatments, databases, quantification and peak fitting. *I4P* is complementary to all available softwares while offering specific potentialities (see below). But its main interest lies in the free availability of the source codes, thus allowing the user to check, modify, adapt and extend it for its own needs. Originally developed for easy and reliable fit of core level spectra from unmonochromated sources that was missing to the author in all the available tools, *I4P* has been progressively enriched towards HAXPES applications in terms of databases of binding energies and photo-ionisation cross sections or depth-profiling by inelastic background analysis or angle-resolved photoemission. Furthermore, all equations and references to the relevant literature are carefully given in the user manual.

This article is organized as follows. All the functionalities of *I4P* are introduced one after the other by stressing on the specificity of the implementation: (i) basic data analysis (Sect. 3), (ii) associated databases (Sect. 4) of binding energies, photo-ionization cross sections, (in)elastic mean free paths and effective attenuation lengths, (iii) quantification using elastic peaks (Sect. 5.1) and depth-profiling with angle-resolved photoemission (Sect. 5.2), inelastic background analysis (Sect. 5.3) and (iv) peak fit and related options (Sect. 6). Examples of *I4P* capabilities for peak analysis and quantification are given on the fly.

2. Code structure and data handling/format

I4P is organized in the form of a global interactive menu which items will be detailed in turn in the following sections. Each of them corresponds to an *Igor Pro* ASCII procedure which can be modified by the user. Spectra are stored by evenly spaced increasing binding energy or energy loss (units eV) in the form of a 1D scaled vector, the so-called "waves" in the *Igor Pro* language [38]. *I4P* is able to read ASCII photoemission data, in either the (*.vms) VAMAS [39], the (*.xy) SpecLabProdigy or the (*.txt) EIS Omicron format. Even if other formats can be easily handled by the user, tools are offered (i) to convert binding energy/intensity columns to a formatted wave which is internally compatible with *I4P* and (ii) to merge properly spectra. All available information contained in the input file (such as excitation energy, energy step, instrument, pass energy, etc...) are included as internal wave notes which are propagated across all calculations. For each spectrum, binding energy, response function and data corrected from the latter can be created at loading or later on. Data are systematically normalized to the number of sweeps and the counting time (units cps). To help the user, all new spectra produced by data treatment are labelled with specific documented wave extensions. At last, as integration and convolution required in many data treatments (such as background subtraction; see below) are performed numerically, the results may depend on energy step and range; spectrum oversampling by cubic spline interpolation, possible with simple internal commands, is advised for meaningful calculations.

3. Basic data analysis

3.1. Spectra overlap

Beyond all the internal plotting capabilities of *Igor Pro* and an easy conversion between kinetic and binding energies (E_K/E_B) on a given graph, *I4P* offers a very useful peak overlap option to visually and qualitatively compare spectra line shapes. On a given graph, it will offset and renormalise all the plotted spectra on a given master one selected through cursors. Three overlap options are possible: (i) on the background (at the low binding energy side of the peak) and on the position/maximum of the peak located in between cursors, (ii) on the background through subtraction, (iii) on the background through a multiplication and (iv) on the background and on the peak position/area. Resulting spectra differences can be calculated over their common binding energy range. Although trivial at a first sight, this overlapping option allows highlighting differences in a series of spectra, such as a physical peak shift, a charge effect or a change in chemical components. This automated graphing option corresponds somehow to a "quick" background subtraction and peak analysis.
Using cursors to define peaks, it is also possible to calculate Auger parameter and a first estimate of peak characteristics (area, position, full-width at half maximum (FWHM), etc...). Easy change of E_B origin due to improper calibration of the analyser work function or charge effect is also possible.

3.2. Deconvolution of source satellites

In the case of laboratory photoemission set-ups not equipped with a monochromator, the core level excitation from the satellite lines of the source may lead to erroneous interpretations in terms of actual chemical components, especially for core levels with a large spin-orbit splitting. For the most common laboratory sources (Mg-Kα, Al-Kα or He I/II), *I4P* offers the possibility to remove these satellite features through an actual deconvolution via Fourier

transform or through a simple subtraction. The overall resolution function is defined as a sum of lorentzian peaks corresponding to the lifetimes of $K\alpha_{1,2,3,4,5,6} - K\beta$ lines in XPS or to He I/II$_\alpha, \beta, \gamma$ in UPS, convoluted by an apparatus gaussian function of given full-width at half-maximum (FWHM). The relative intensities, positions and widths of all these satellites are extracted from Refs. [40–43]. During this treatment, the apparent resolution can also be improved by dividing in Fourier space by the gaussian instrumental function using Wiener filtering [44] to prevent noise amplification. This latter is estimated through fitting over a moving window. The final spectrum is reconvoluted either by a Dirac peak, by the Kα_1 line only or by the Kα_1+Kα_2 line sum. The case of other unmonochromated sources can be easily handled if the relative positions and intensities of satellites are known. In the case of the Al/Mg dual anode source, contamination of the target by a foreign element (cross talk, target oxidation, excitation of Cu support) may happen to a given extent. The correction from the corresponding main ghost lines (Al-Kα, Mg-Kα, O-Kα, Cu-Kα) can be performed with *I4P* by simple subtraction and their relative contributions determined. At last, one should keep in mind that removal/deconvolution of satellite/ghost lines is not valid for Auger transitions.

3.3. Inelastic background subtraction

All photoemission features, core level peaks and Auger transitions, are overlapped with a background signal due to electrons that have suffered from energy losses. It depends not only on the dielectric functions of the materials crossed by the photoelectrons but also on the concentration profile of the probed element and the sample morphology. This latter aspect of inelastic background analysis will be treated in Sect. 5.3. Various accounts of inelastic background have been developed over the years with their own effectiveness and limitations. Background subtraction is a mandatory step in estimating elastic peak areas which are at the heart of quantification in photoemission (see Sect. 5.1-5.2). It is often performed prior to peak fitting (at the opposite to *I4P*; see Sect. 6.2) leading to a well-commented user bias in the analysis [45, 46]. Inelastic background removal can be performed with *I4P* in a very versatile way using different models. By defining the measured spectrum $M(E_B) = S(E_B) + B(E_B)$ as the sum of elastic spectrum $S(E_B)$ and an inelastic background $B(E_B)$, the available background models are given by:

- Linear: linear background.
- Shirley integral background [47, 48]:

$$B_{Sh}(E_B) = S_h \int_{E_B^0}^{E_B} S^*(E'_B) dE'_B, \qquad (1)$$

  where $S^*(E_B) = S(E_B) - S(E_B^0)$. E_B^0 is chosen on the low binding energy side of the peaks.

- Generalized Shirley background following the slope background of Ref. [49]:

$$\begin{aligned} B_{GSh}(E_B) &= S_h \int_{E_B^0}^{E_B} S^*(E'_B) dE'_B \qquad (2) \\ &+ S_l \int_{E_B^0}^{E_B} dE'_B \int_{E_B^0}^{E'_B} S^*(E''_B) dE''_B \\ &+ S_c \int_{E_B^0}^{E_B} dE'_B \int_{E_B^0}^{E_B\prime} dE''_B \int_{E_B^0}^{E''_B} S^*(E'''_B) dE'''_B. \end{aligned}$$

  It allows for a greater flexibility in the account of the post-peak background line shape.

- Tougaard integral background with a 2 or 3 parameter inelastic electron scattering cross section (IESCS) [4, 50, 51]:

$$\begin{aligned} B_{Tg}(E_B) &= \int_{E_B^0}^{E_B} \lambda_i K(E_B - E'_B) M^*(E'_B) dE'_B \\ \text{with} \quad \lambda_i K(T) &= \frac{B(T-G)\Theta_H(T-G)}{[C + (T-G)^2]^2} \\ \text{or} \quad \lambda_i K(T) &= \frac{B(T-G)\Theta_H(T-G)}{[C - (T-G)^2]^2 + D(T-G)^2}. \qquad (3) \end{aligned}$$

  Parameters B, C, D are fixed at tabulated values from Refs. [4, 50–53] (either universal $B = 3006$ eV^2; $C = 1643$ eV^2 or specific for coinage/transition metals, Si, Ge or polymers) or given by the user. G is the material gap, if any, and $\Theta_H(x)$ the Heaviside function [$\Theta_H(x) = 0$ if $x < 0$ and $\Theta_H(x) = 1$ if $x \geq 0$].

- distorted Shirley background [54, 55] with user given parameters B, C, D, G:

$$\begin{aligned} B_{DSh}(E_B) &= \int_{E_B^0}^{E_B} \lambda_i K(E_B - E'_B) M^*(E'_B) dE'_B \quad (4) \\ \text{with} \quad \lambda_i K(T) &= \frac{B\left[1 - \exp\left[-D(T-G)\right]\right]}{C + (T-G)^2} \Theta_H(T-G) \end{aligned}$$

  It corresponds to the generalization of the IESCS associated to the Shirley background.

- A blend of all of them.

The background, subtracted between two binding energies $E_B^0 < E_B^1$ indicated by cursors on a spectrum, is either calculated from the user/tabulated parameters or pinned on the corresponding spectrum values (*i.e.* $B(E_B^0) = B(E_B^1) = 0$). In the latter case, a self consistent loop is applied to determine the corresponding scaling factor (S_h, B, B_s) until an internal threshold of 10^{-3}. To obtain more physical results, averaging around the end points is performed over a given window in energy and the background is eventually forced to be positive by automatically adjusting the ending value. Nevertheless, the adaptation

of this prefactor requires a higher signal at E_B^1 than at E_B^0. At last, a polynomial background interpolated on data points before the considered peak can be subtracted prior to the calculation of the integral background.

3.4. Intensity-energy response function

In principle, photoemission spectra should be corrected from the intensity/energy response function $R_F(E_K)$ (sometimes called transmission function) of the whole instrument. This correction is of paramount importance when determining element concentrations from elastic peak areas, in particular for features far apart in kinetic energy. For an aberration-free hemispherical analyser with an homogeneous sample illumination, it scales as $R_F(E_K) \propto 1/E_K$ in fixed analyser transmission (FAT; constant pass energy E_p) or as $R_F(E_K) \propto E_K$ in fixed retardation ratio (FRR, constant $K = E_K/E_p$). *I4P* implements corrective distortions in $R_F(E_K)$ via an *ad hoc* energy dependent exponent $R_F(E_K) \propto 1/E_K^{n(E_K)}$ in FAT and $R_F(E_K) \propto E_K^{n(E_K)}$ in FRR in the form of:

$$\begin{aligned} n(E_K) &= \sum_{k=0}^{6} n_k \left[E_K\right]^k \\ n(E_K) &= n_0 + n_1 \tanh\left[\frac{E_K - n_2}{n_3}\right] \\ n(E_K) &= n_0 + n_1 \mathrm{erf}\left[\frac{E_K - n_2}{n_3}\right], \end{aligned} \quad (5)$$

where n_k are constants and $\mathrm{erf}(x) = \frac{2}{\sqrt{\pi}} \int_{-\infty}^{x} \exp(-t^2)dt$. Several methods reviewed in Ref. [18] have been proposed to determine $R_F(E_K)$. The quantified peak area approach (QPA) relies on the comparison of peak areas of several reference materials (*e.g.* Ag, Au, Cu) to calculated relative sensitivity factors [56]. In the survey spectra approach (SSA), a metal reference spectrum acquired on a metrology spectrometer at National Physical Laboratory [57–59] is compared to a measurement to get $R_F(E_K)$; unfortunately, the associated NPL software is no longer available. The procedure implemented in *I4P* is based on the analysis of the inelastic background of a survey spectrum of selected metals [18, 60]. In the same spirit as in the work done on instrument calibration with polyethylene [61–63], the method assumes that the background in between core levels and Auger transitions is accurately described by the universal Tougaard IESCS (Eqs. 3). Using an initial set of parameters n_k in Eqs. 5, the measured spectrum $M(E_K)$ is corrected from $R_F(E_K)$ to get the corrected spectrum $I(E_K) = M(E_K)/R_F(E_K)$ to which the background $B(E_K)$ can be subtracted using Eqs. 3 to obtain the primary spectrum $S(E_K) = I(E_K) - B(E_K)$. A cost function that quantifies the agreement between $S(E_K)$ and $B(E_K)$ in between photo-excited features is then minimized to obtain n_k. At the iteration j of optimisation, it is defined by:

$$\mathcal{A}_j(n_i, \kappa) = \frac{1}{\omega_j} \int |S(E_K)| dE_K, \quad (6)$$

where ω_j is the fraction of points for which $S(E_K)$ is below noise defined as $\kappa\sqrt{I(E_K)}$ ($\kappa > 0$) . The bias induced by the ω_j-term and the absolute value in Eq. 6 helps improving convergence [18]. The minimisation is performed with the algorithm implemented in *Igor Pro* (Line search; Dogleg; More-Hebbon) or by simulated annealing. Aside user-given or tabulated universal IESCS parameters [4, 50–53], the actual $\lambda_i K(T)$ functions for Ag and Au [51, 64, 65] are also available. The implemented algorithm can be applied simultaneously up to five survey spectra, taken on different materials but in similar measurement conditions, to constrain the $R_F(E_K)$ search by involving photo-excited features spread over a large kinetic energy range. The minimisation is thus performed of the sum of their $\mathcal{A}_j$.

3.5. Mass scale in ion scattering spectroscopy

In the case of ion scattering spectroscopy (ISS), also known as low energy ion scattering (LEIS), an incident ion (usually He^+) of kinetic energy E_K and mass m bounces off the sample surface and transfers a fraction of its energy to the surface atoms of mass M. By analysing the energy loss ΔE_K at a given scattering angle θ_s with an hemispherical analyser, the conservation of momentum and energy [66] gives the mass of the surface atoms. *I4P* offers a convenient tool to convert automatically ΔE_K into mass scale:

$$\frac{M}{m_0} = \frac{1}{1-u}\left[u + 1 - 2\sqrt{u}\cos\theta_s\right] \quad (7)$$

with $u = 1 + \frac{\Delta E_K}{E_K}$.

4. Databases

4.1. Energies of core levels and Auger transitions

An interactive periodic table (Fig. 1) is proposed to identify core level peaks and Auger transitions. For the selected x-ray source (He I/II, Al-Kα, Mg-Kα, Ag-Lα, Cr-Kα, Ga-Kα including their satellites and ghost lines for unmonochromated anodes), labelled ticks are overlapped on a spectrum; their heights are proportional to the relative sensitivity factors (RSF) of core levels and their positions in energy correspond to tabulated values for pure elements [67, 68]. The RSFs are defined in this context as the product (i) of the photo-ionization cross section (PICS) from Refs. [12, 13, 35] corrected from the asymmetry at the a given angle between unpolarized source and analyser and (ii) of the response function of the analyser given by $1/E_K^n$ where n is the fixed exponent; no inelastic mean free paths or effective attenuation lengths are accounted for in those RSFs. The databases used are (i) from Refs. [67, 68] for binding/kinetic energies, satellites, ghost lines and from Ref. [35] for PICS and asymmetry parameters if the photon energy is lower than Al-Kα excitation (1486.6 eV) or (ii) from Ref. [68] and Refs. [12, 13], respectively, for higher photon values. In the case of Auger transitions, only the low energy Auger ones are tabulated [67].

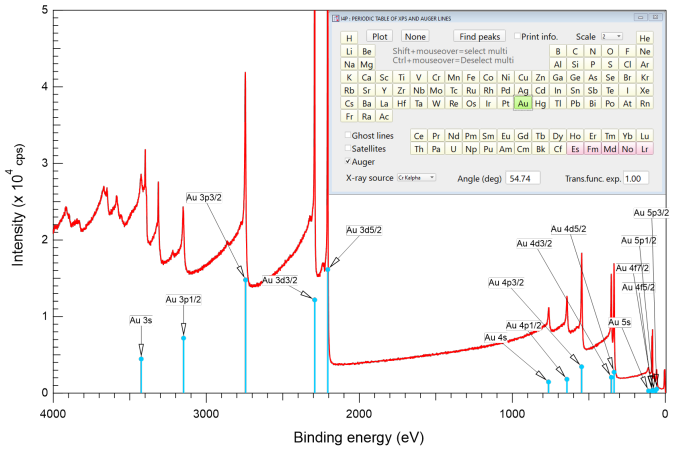

Figure 1: Identification of core levels from the periodic table tool in the case of Cr-Kα HAXPES survey spectrum of Au [69].

4.2. Photo-ionization cross sections

For a selected photon energy $h\nu$, an interactive window (Fig. 2) is available in *I4P* to calculate the photo-ionization cross sections of core levels of all chemical elements using different databases [12, 13, 34–36]:

- Scofield [34] : $h\nu = 1 - 1500$ keV but without account of asymmetry parameter;
- Yeh and Lindau [35] : selected x-ray sources and energies [$h\nu = 10.2$ (H), 16.7 (Ne-I), 21.2 (He-I), 26.8 (Ne-II), 40.8 (He-II), 80, 132.3 (Y-Mζ), 151.4 (Zr-Mζ), 200, 300, 600, 800, 1041.0 (Na-Kα), 1253.6 (Mg-Kα), 1486.6 (Al-Kα) and 8047.8 (Cu-Kα) eV];
- Trzhaskovskaya and Yarzhemsky [12, 13] : $h\nu = 1.5 - 10$ keV sampled every keV;
- Cant and *al.* [36] : $h\nu = 1.5 - 10$ keV expressed as interpolation formulas over several references [12, 13, 34, 70].

For a given core level, values of the cross section σ, the dipolar asymmetry β, non-dipolar terms of first order (γ, δ) and of second order $(\Delta\beta_{unpol}, \Delta\beta_{lp}, \eta, \mu, \xi)$ in $\mathcal{O}(kr)$ are extracted from the digitized versions Refs. [71–75] of databases Refs. [12, 13, 34, 35, 76]. If the selected photon energy (or x-ray source) is not directly available in the databases, a simple linear interpolation is made over available values. Besides these values, the outputs are the binding energy of the considered core level from Refs. [67, 68], the level occupancy, the spectroscopic factor from Ref. [77] (ratio between white line and shake-up satellites), the actual photo-ionization cross section $\Sigma = \frac{\sigma}{4\pi}(1 + F)$ (either in kbarn or its normalized value to C 1s for an Al-Kα source at the magic angle). The total asymmetry factor F is also given; it depends on (i) the polarization state of the source (unpolarized, monochromator, circular, partial [62]) and on (ii) the relative orientation of the source, the sample and the analyser (see Ref. [36] and erratum). The latter is defined through several angles: (i) ψ between the x-ray source and the emission direction; at the magic angle ($\arccos 1/\sqrt{3} = 54.73°$), the dipolar asymmetry is zero; (ii) the dihedral angle ζ between the monochromator-sample-analyser plane and the anode-monochromator-sample plane (see Ref. [62]); (iii) the spherical coordinates θ_x, ϕ_x (deg) of the electron emission direction from the electric field direction (z-axis) for partial polarization (see Refs. [12, 13]). In the case of an unpolarized source, as used in most cases,

$$\begin{aligned} F &= -\left[\beta + \frac{\Delta\beta_{unp}}{4}\right](3\cos^2\psi - 1) \\ &- \left(\delta + \frac{\gamma}{2}\sin^2\psi\right)\cos\psi \\ &+ \frac{\xi}{8}(35\cos^4\psi - 30\cos^2\psi + 3). \end{aligned} \quad (8)$$

The implemented "monochromator" option corresponds to a partial beam polarization due to Bragg reflection on most-common monochromator crystals employed for usual emission lines [62] (*e.g.* α-$SiO_2(10\bar{1}0)$ for Al-Kα). The options of circular or partial polarizations (with ratio $0 < P < 1$) are useful for synchrotron radiation.

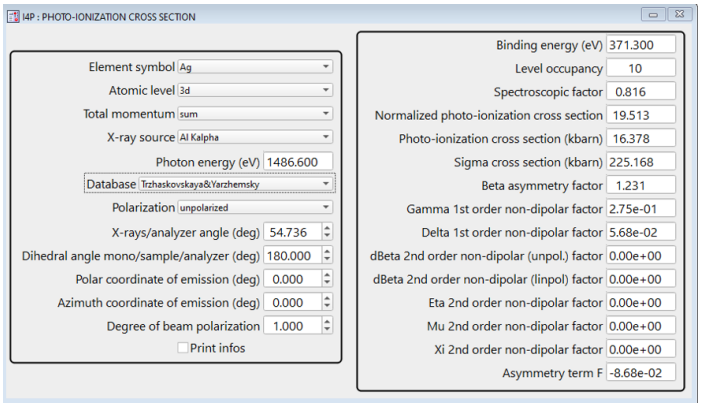

Figure 2: Interface panel with photo-ionization cross section databases [12, 13, 34–36, 76, 77]. Chemical element, core level, x-ray source/photon energy, polarization state can be selected from drop-down menus in the left panel. All outputs are given in the panel on the right.

4.3. (In)elastic mean free paths and effective attenuation lengths

Quantification in photoemission (see Sect. 5) requires the evaluation of several lengths that characterize the inelastic and elastic transport of the photoelectron in matter (see reviews for their definitions [7–11]) . Starting from an internal database of elemental materials, common semiconductors and oxides (including material density, molar mass, number of valence electron, gap, atomic numbers of material constituents), an *I4P* interactive panel (Fig. 3) provides at a selected kinetic energy:

- the inelastic mean free path (IMFP) λ_i using predictive formulas fitted on more extensive dielectric calculations [TTP-2M [33, 78–80] (E_K = 50 eV-200 keV), Gries [81], Seah [82] (E_K = 100 eV-10 keV), JPT [6] (E_K = 50 eV-200 keV), TPP-LASSO-S [83]];
- the transport mean free path (TRMFP) λ_{tr} calculated from the effective correction to the analytical expression of the transport cross-section based on partial-wave expansion (E_K = 50 eV-30 keV) [84–86]; by including "high" angle scattering, λ_{tr} differs from the elastic mean free path λ_e [87];
- the albedo factor $\omega = \lambda_i/(\lambda_i + \lambda_{tr})$ used in the kinetic Boltzmann equation in the transport approximation [7–9, 88];
- the mean escape depth (MED) [89] and the effective attenuation lengths (EAL) of a bulk, a film of a given thickness and a marker buried at a given depth as defined and detailed in Refs. [9–11].

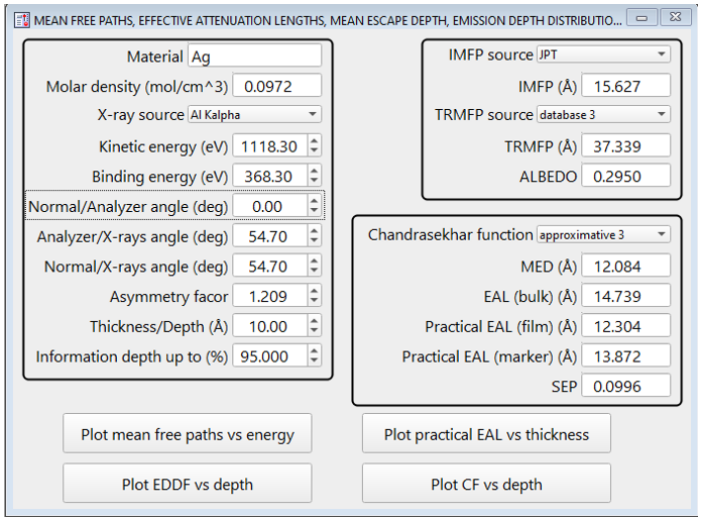

Figure 3: Interface panel with databases of mean free paths, effective attenuation lengths and emission depth distribution function. The example here corresponds to the Ag 3d core level in bulk Ag at Al-Kα (E_K = 1118.3 eV).

The angles α, ψ, θ (deg) between sample normal/analyser, analyser/x-ray, sample normal/x-ray directions respectively, as well as the asymmetry factor β [12, 13, 35] of the considered core level, are required in the calculations of EALs [7–11, 88]. Note that calculations in the transport theory are valid for unpolarized sources only; non-dipolar corrections to EALs were found negligible except at high kinetic energy and grazing emissions [90, 91] and are not accounted for herein. Calculations can be performed within different levels of approximations for the Chandrasekhar function that is central in the kinetic Boltzmann equation [9, 88, 92–95]. While displayed values are calculated at a given kinetic energy or thickness/depth (Fig. 3), all quantities can be plotted as a function of these variables but at the expense of CPU time (Fig. 4). In particular, in the case of a film, the plot of EALs as function of thickness/depth gives access to the average value and the information depth (ID) defined up to a threshold given by the user [9, 10]. The emission depth distribution function (EDDF) [9, 10] and the ratio of EDDF with to without elastic scattering (the so-called CF function) [96] can also be directly visualized. Also, the surface excitation parameter (SEP) S, which characterizes the photoelectron losses due to the material/vacuum interface [$\exp(-S)$ damping], is evaluated with the effective formulas of Refs. [8, 97, 98]. To conclude, this interactive calculator is somehow complementary to QUASES-IMFP-TPP2M [33], NIST [10], SESSA [31], TRANS_APPROX [99] softwares for IMFP/EAL calculations.

5. Quantification

5.1. Quantification from elastic peak areas

Based on elastic peak areas obtained after a proper inelastic background removal (Sect. 3.3) or adequate peak fitting (Sect. 6), several interactive panels are provided to determine [10, 100, 101] (i) a film thickness from the ratio of film to substrate lines or from the relative damping in the film of two substrate lines recorded at different kinetic energies or (ii) the composition of a perfect semi-infinite alloy with an arbitrary number of components (Fig. 5) as done in most available softwares. In the case of a film, three geometries are encompassed (Fig. 5): (i) a continuous layer geometry, (ii) pancakes of constant thickness or (iii) hemispheres of equal radius covering a fraction of the surface (Fig. 5). Calculations are performed at a fixed emission angle and do not account for shadowing effects in nanostructures. In the case of a continuous film of thickness t (Fig. 5-a), used as an example herein, the elastic areas of substrate A_s and film A_f core levels scale as:

$$A_s \propto n_s \sigma_s R_s \lambda_{ss}^{eb} \cos(\alpha) \exp\left(-\frac{t}{\lambda_{sf}^{ef}\cos\alpha}\right) \quad (9)$$

$$A_f \propto n_f \sigma_f R_f \lambda_{ff}^{eb} \cos(\alpha) \left[1 - \exp\left(-\frac{t}{\lambda_{ff}^{ef}\cos\alpha}\right)\right]$$

where, for the substrate (s) and film (f), $n_{s,f}$ are the known atomic concentrations, $\sigma_{s,f}$ the photo-ionisation cross sections (Sect. 4.2), $R_{s,f}$ the response functions at the corresponding kinetic energies, α the emission angle and $\lambda_{pq}^{e} = \lambda_{ff}^{eb}, \lambda_{ss}^{eb}, \lambda_{sf}^{ef}, \lambda_{ff}^{ef}$ the effective attenuation lengths of the photoelectron from core level p in the material q [the superscripts (eb, ef) correspond to bulk or practical film EAL [9, 102] (see Sect. 4.3), in principle averaged over thickness up to the information depth]. Expressions for the other geometries of Fig. 5 are given in the manual. Note that the account of elastic scattering effects in the

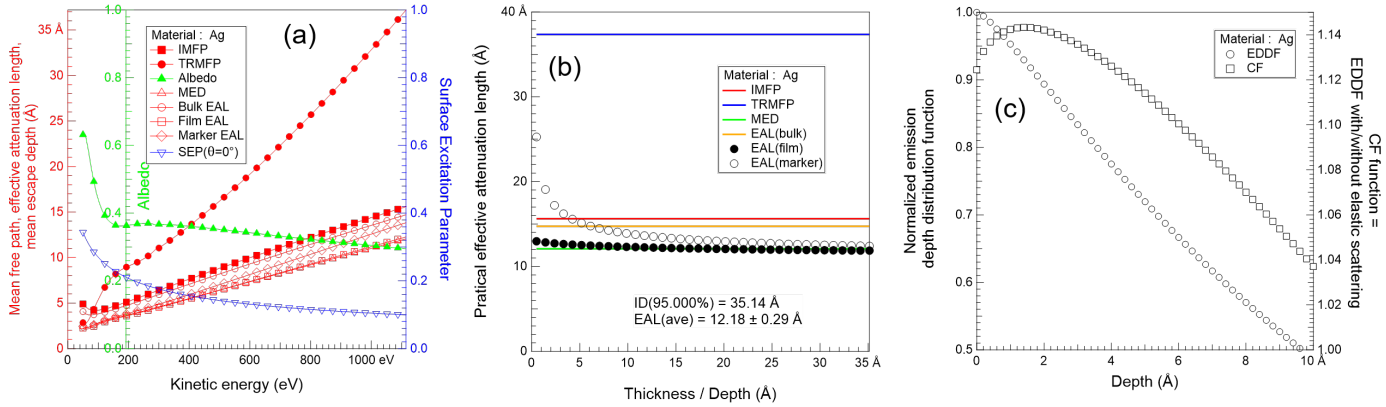

Figure 4: Example for Ag: (a) IMFP, TRMFP, albedo, EALs, SEP as a function of kinetic energy, (b) EALs for film and marker as a function of thickness/depth and (iii) EDDF and CF versus depth. See Refs. [8–10] for definitions.

case of a film morphology requires the calculation of several characteristic lengths λ^e_{pq} [9, 102]. If they are replaced simply by the corresponding IMFPs as usually done, elastic scattering effects are thus ignored. Eventually, a further correction by an excitation term $\exp(-S)$ can be accounted for at each interface crossed by the photoelectron. Its calculation requires advanced dielectric simulations for each interface [29] and an effective formula [8, 97, 98] has only been derived up to now for the bulk/vacuum interface (see interactive panel Fig. 3). Once all these parameters are entered, the transcendental equation in thickness given by the measured A_f/A_s ratio (Eq. 9) is solved by dichotomy until a given accuracy. In the case of the alloy model (a), the direct proportionality of peak areas to RSFs and atomic concentration [*i.e.* $A_q \propto x_a \sigma_a R_a \lambda^{eb}_{aa} \cos(\alpha)$] allows for a straightforward determination of the relative concentration x_a of all elements. At last, note that, owing to the definition of PICSs, elastic peak areas should contain, not only the main core level line, but also all its shake and multiplet splitting satellites [25, 101].

5.2. Angle-resolved photoemission analysis

Angle-resolved photoemission (ARXPS) and its Auger spectroscopy counterpart (ARAES) are well-established procedures to determine film thicknesses, and more generally the in-depth distribution of an element in the surface region, but at rather modest in-depth resolution without any *a priori* knowledge on the profile [103, 104]. It consists in analysing the variation of elastic peak intensities $A(\alpha)$ as a function of the emission angle α. It is more suited for polycristalline or amorphous samples, for which specific photodiffraction effects are averaged, with low roughness as handling shadowing effects [103] is not trivial. In the historical ARXPS geometry, the sample is mounted on a rotating manipulator in front of the analyser at fixed incoming x-rays (Fig. 6-b). With the advent of 2D detector and large aperture hemispherical analysers, the non energy-dispersive direction of the apparatus can be used to map the α-dependence of core levels (Fig. 6-b). Both

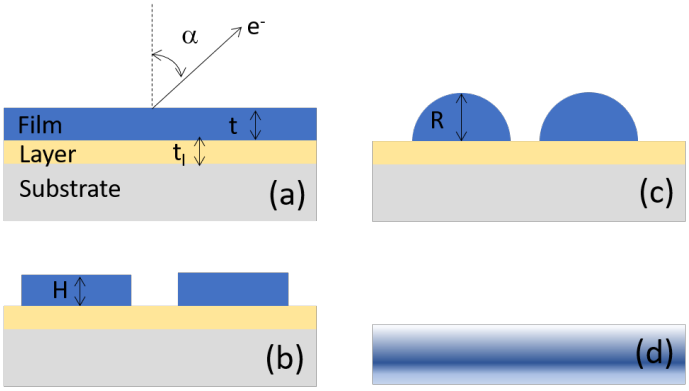

Figure 5: Morphologies available in *I4P* in the case of quantification from elastic peak areas at fixed emission α: (a) continuous thin film of thickness t; (b) film of pancakes of similar height H; (c) film of hemispheres of similar radius R; (d) homogeneous alloy. The substrate may be covered by a continuous layer of thickness t_l in some cases. For discontinuous films, the surface covered by the objects is required in the calculation.

geometries differ in terms of variation with α of the angles ψ and θ between x-ray/detection and x-rays/sample normal directions, respectively. The *I4P* suite provides a dedicated tool for the ARXPS analysis of a stack with an arbitrary number of (dis)continuous layers (Fig. 6-a). It is similar to available softwares (*QUASES-ARXPS* by S. Tougaard [105], StrataPHI by *PhysicalElectronics*, Avantage by *ThermoFisher Scientific*) but with extra-features such as the exact treatment of elastic scattering in the Boltzmann transport approximation [7, 9, 11, 88], the account of the finite analyser aperture or of the scattering geometry.

For an element distributed in a matrix with an in-depth concentration profile $c(z)$, the measured photoemission elastic intensity reads:

$$I \propto \int_0^\infty c(z)\phi(z,\alpha)dz = \int_0^\infty c(z)CF(z,\alpha)\exp\left(-\frac{z}{\lambda_i\cos\alpha}\right)dz, \tag{10}$$

where $\phi(z,\alpha)$ is the so-called emission depth distribution function (EDDF) [7–9, 11]. Without elastic scattering, the EDDF is simply given in the straight line approximation (SLA) by $\phi^{nel}(z,\alpha) = \exp[-z/(\lambda_i\cos\alpha)]$ with a signal damping driven by the electron inelastic mean free path λ_i. A correction function CF has to be introduced to account for elastic scattering effects in the photoelectron transport. Even in the simple case of a continuous layer on a substrate, ignoring them can lead to a sizeable error in the determination of the film thickness in ARXPS, an effect that can mitigated when using bulk EALs instead of IMFPs in SLA [106]. However, the solution of the kinetic Boltzmann equation in the electron transport theory [7, 9, 11, 88] provides an estimate of CF that compares fairly well to Monte-Carlo simulations despite its angular averaging of the elastic scattering cross section. Although involved and time-consuming, this approach of CF calculation is offered in *I4P*. Fortunately, approximate and lighter expressions of CF tested intensively against Monte-Carlo simulations have been derived by Jablonski and Tougaard [107, 108] and Nefedov and Federova [7, 109]. When used, the latter are accurate down to ~ 5 % in terms of thickness [106]. Both models, included in *I4P*, imply the knowledge of the transport mean free path λ_{tr} [or equivalently of the albedo $\omega = \lambda_i/(\lambda_i + \lambda_{tr})$] but also of the dipolar asymmetry factor β of the considered core level. These quantities can be easily obtained with *I4P* (see Sect. 4.3 and 4.2).

Approximations are also necessary to tackle the case of a multilayer. The elastic signal damping D_n in layer n of thickness t_n buried at depth h_n in a multilayer (see Fig. 6-a) reads simply:

$$D_n = \exp\left(-\frac{t_n}{\lambda_{i,n}\cos\alpha}\right), \tag{11}$$

in SLA and can be approximated by (see Ref. [106] for details):

$$D_n = \frac{\phi_n(t_n + h_n, \alpha)}{\phi_n(h_n, \alpha)} \tag{12}$$

when elastic scattering is included through $\lambda_{tr,n}/\omega_n$ of the layer with the chosen EDDF description. Thus, if the element is present at a relative concentration c_n, the integrated intensity emitted from layer n is given, exactly in SLA and approximatively otherwise, by:

$$A_n = c_n \int_0^{t_n} \phi_n(z,\alpha)dz \prod_{k=0}^{n-1} D_k. \tag{13}$$

The total intensity from a given element in the multilayer reads $A_{tot} = \sum_{n=0}^{N_l-1} A_n$. The case of partial coverage f_n in each layer can also be handled easily provided that shadowing effects are ignored *i.e.* that emission is not too grazing. At last, x-ray beam and detection footprints give rise to $1/\cos\theta$ and $1/\cos\alpha$ corrections to A_{tot} while the finite-aperture of the analyser $2\Delta\alpha$ can be accounted for through an average over the α-window.

As absolute measurements are untractable, an internal normalization to the sum of the N_α data points is systematically made in *I4P* to compare actual experimental data $A^e(\alpha)$ and theoretical calculation $A^t(\alpha)$. Yet, a χ^2_f criterion:

$$\begin{aligned}
\chi^2_f &= \frac{1}{N_\alpha}\sum_{k=1}^{N_\alpha}\left[\frac{R^e(\alpha_k) - R^t(\alpha_k)}{\sigma_{R^e}(\alpha_k)}\right]^2 \\
R^e(\alpha_k) &= \frac{A^e_s(\alpha_k)}{A^e_r(\alpha_k)} \\
R^t(\alpha_k) &= \frac{A^t_s(\alpha_k)}{A^t_r(\alpha_k)} \\
\sigma_{R^e}(\alpha_k) &= R^e(\alpha_k)\left[\frac{\sigma_s(\alpha_k)}{A^e_s(\alpha_k)} + \frac{\sigma_r(\alpha_k)}{A^e_r(\alpha_k)}\right].
\end{aligned} \tag{14}$$

on the ratio of areas between the studied sample (s) and a reference (r) is actually used to seek for the best parameter set accounting for experimental error bars (σ_s and σ_r, respectively). Several choices of $A_r(\alpha)$ used in χ^2_f definition are possible in *I4P*: (i) $A_r(\alpha) = 1$ which reverts to fit only the experimental ARXPS data, (ii) that corresponding to a bulk semi-infinite material and (ii) that of an internal reference core level in the multilayer with a known concentration profile, most of the time taken as coming from substrate. This last relative normalization (iii) is much effective than the two former ones (i)(ii) as it allows to get rid of unknown variations from angle to angle such as the x-ray flux. With the provided *I4P* tool, although time-consuming, the search of the global χ^2_f minimum is performed randomly over a finite fraction of the $(t_n, c_n, f_n, \lambda_{i,n}, \lambda_{tr,n})$ parameter space. Depending on the option of referencing, the best results for the data, the reference and their ratio are plotted as well as the corresponding concentration profiles and coverage (Fig. 7). χ^2 and R_b reliance factors (see Eq. 20 for definitions) for the reference and the sample are also by-products. Without any *a priori* knowledge of the concentration profile, a Tikhonov regularization

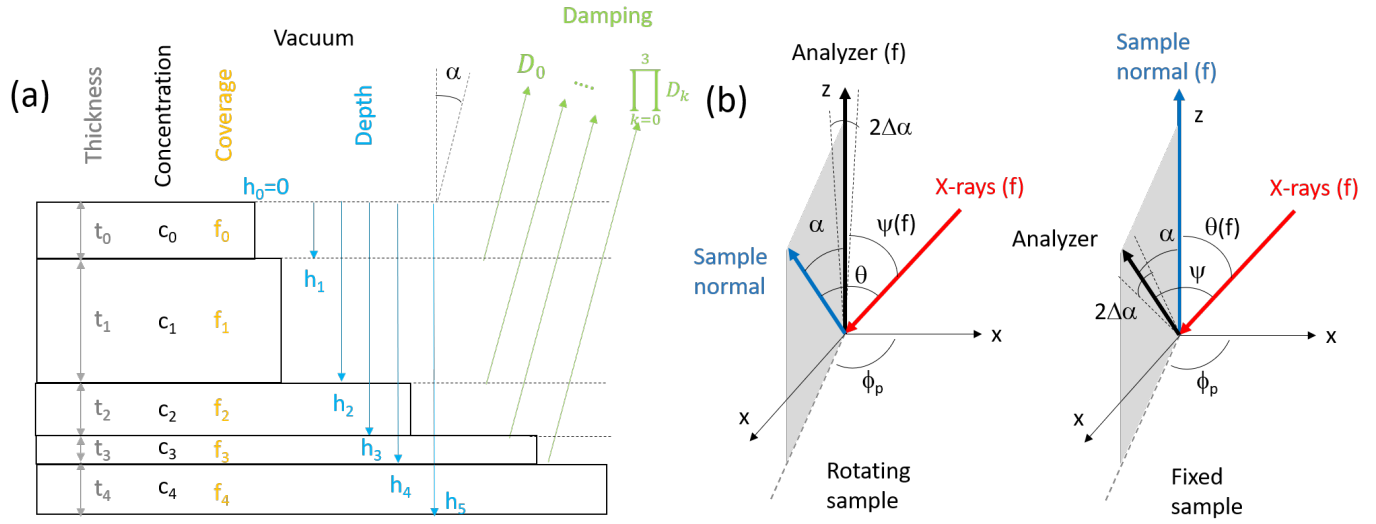

Figure 6: Angle-resolved photoemission analysis: (a) multilayer scheme with a stair step morphology and (b) measurement geometries corresponding to (i) a rotating sample and a fixed analyser or to (ii) a fixed sample and a wide-aperture detection. The variations of the angles θ and ψ with α differ in the two geometries. (f) stands for fixed and $\Delta\alpha$ for the analyser finite aperture.

term [103, 104] proportional to $\int_0^\infty (\partial c(z)/\partial z)^2 dz$ can be added to χ^2_f to favour convergence towards less spiky and smoother profiles.

Fig. 7 shows an example of ARXPS analysis of a self-limited alumina oxide film obtained by high-temperature O_2 exposure ($T = 1173$ K, $p \simeq 2.10^{-7}$ mbar) of a $Fe_{0.85}Al_{0.15}(110)$ random body-centred alloy (see Refs. [110, 111] for all details). The Al 2p core level was measured between normal ($\alpha = 0°$) and grazing emission ($\alpha = 70°$) (Fig. 7-b). This peak presents fingerprints of both the metallic substrate and of the oxide film (Fig. 7-b) which can be separated with an appropriate fit [110, 111] (see Sect. 6 for *I4P* potentialities) and integrated after inelastic background subtraction. In the present example, the oxide film thickness is obtained by fitting the Al 2p oxide/metal area ratio accounting for a subsurface enrichment in Al determined from an analysis of the relative Al 2p and Fe 3p metallic contributions (not shown; see Refs. [111–113]). The better agreement between measurement and simulation on the ratio (Fig. 7-a; blue points and curves) than on raw data (red/green) demonstrates all the interest of the internal normalization in ARXPS. Indeed, raw data are impacted by angular effects of electron collection which are not fully accounted for by simple footprint corrections but which cancel out when using the ratio of two lines. The obtained value of $t \simeq 10$ Å is in close agreement with previous determinations [111, 113] based on an angle-by-angle analysis of ratio of intensities such as done in Sect. 5.1.

5.3. Inelastic background analysis

S. Tougaard and coworkers have demonstrated the interest of using inelastic background analysis (IBA) for depth profiling (see Refs. [4, 5, 114, 115]). Compared to elastic signal that comes at 95 % from a depth of about $3\lambda_i$, the probing depth can be extended up to $8 - 9\lambda_i$ by focusing on the inelastic electron signal. The interest for IBA is renewed by the advent of commercial photoemission set-ups equipped with Cr/Ga-Kα high energy sources that increase significantly the IMFPs compared to more conventional Al/Mg-Kα anodes [116]. An *I4P* menu has been developed for IBA as described theoretically in Refs. [4, 114, 115] and done in the *QUASES-TOUGAARD* software [117]. For an element with in-depth profile concentration $f(z)$, the measured spectrum $M^*(E_B)$ (corrected for the apparatus response function; Sect. 3.4), the intrinsic spectrum $S^*(E_B)$ and the inelastic background $B^*(E_B)$ are theoretically related by [4, 114, 115]:

$$
\begin{aligned}
S^*(E_B) &= \frac{1}{P_1}\left\{M^*(E_B) - B^*(E_B)\right\} \\
&= \frac{1}{P_1}\left\{M^*(E_B) - \frac{1}{2\pi}\int dE'_B M^*(E'_B) \right. \\
&\left. \int ds \exp[-is(E_B - E'_B)]\left[1 - \frac{P_1}{P(s)}\right]\right\} \qquad (15) \\
&= \frac{1}{P_1}\left\{M^*(E_B) - \frac{1}{2\pi}\int dE'_B S^*(E'_B) \right. \\
&\left. \int ds \exp[-is(E_B - E'_B)]\left[P(s) - P_1\right]\right\} \qquad (16)
\end{aligned}
$$

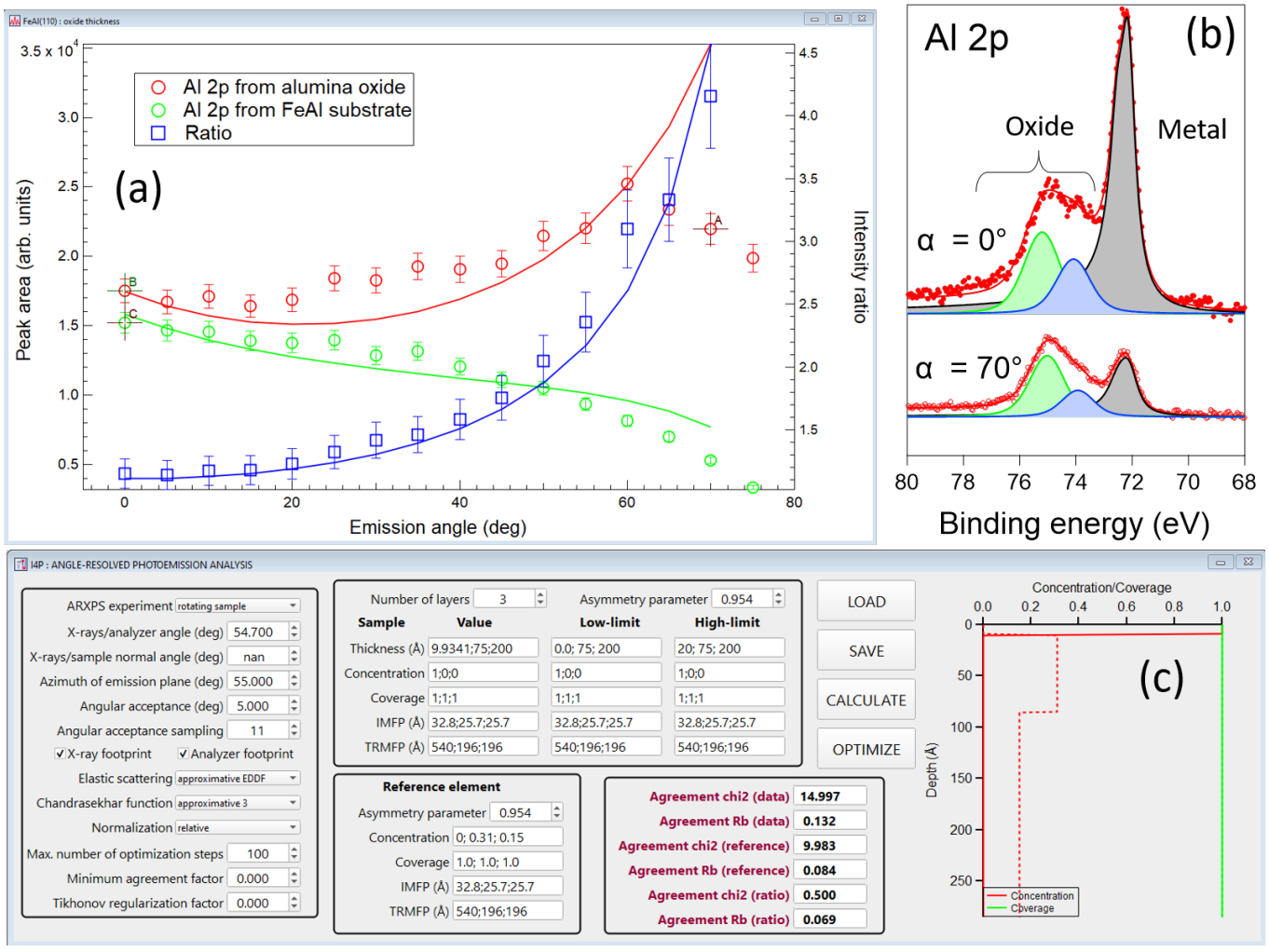

Figure 7: Example of angle-resolved photoemission analysis of an alumina film on a $Fe_{0.85}Al_{0.15}(110)$ crystal. (a) Interactive graph with (i) Al 2p integrated peak area from the alumina film (red symbols; from green and blue peaks in Fig. b) and from the substrate (green symbols; from grey peak in Fig. b) and their ratio (blue symbols) and (ii) their fits with a multilayer model (coloured lines); relative error bars of 5 % are used on data points. (b) Fits of Al 2p core level with components corresponding to the alumina film and the metallic substrate [111, 113]. (c) Interactive panel for setting simulations parameters and the morphologies of the sample and reference multilayers. Final concentration profiles and coverage are plotted on the right and the agreement factors are given in red.

where:

$$\begin{aligned} P_1 &= \int_0^\infty f(z)\exp\left[-\frac{z}{\lambda_i\cos\alpha}\right]dz \\ P(s) &= \int_0^\infty f(z)\exp\left[-\frac{z\Sigma(s)}{\cos\alpha}\right]dz \\ \Sigma(s) &= \frac{1}{\lambda_i}\left\{1-\int_0^\infty \lambda_i K(T)\exp[-isT]dT\right\}. \quad (17) \end{aligned}$$

$\lambda_i K(T)$ is the IESCS corresponding to the embedding matrix and is eventually given by a universal function (Eq. 3). $M^*(E_B), S^*(E_B), B^*(E_B)$ correspond to signals corrected from background on the low binding energy side of the elastic peak (see below). The available profiles in *I4P* correspond to the various nano-structure morphologies depicted in Fig. 8 [37]; $f(z)$ depends on the material concentration c and on a set of geometrical parameters such as layer thickness Δz, burying depth z_0 or surface coverage f. Compared to literature [117], the modellings have been extended towards truncated spheroidal or conical particles either at the surface or buried at a given depth. For all of these profiles, if the photoemission spectrum $M_r(E_B)$ of a reference sample of known composition profile and with a concentration c_r is used in the analysis (see below), the relative concentration c/c_r can also be determined. Nevertheless $M_r(E_B)$ should be measurement in exactly the same conditions as $M(E_B)$.

Fig. 9 shows an example of IBA for the Ag 3d core level from Ag nanoparticles recorded with an unmonochromated Al-Kα source at an emission of $\alpha = 24.5°$; islands were grown on an oxidised Si wafer by sputtering deposition (see Ref. [118] for details). An ancillary measurement on a continuous thick film was performed with the same apparatus settings to have a bulk Ag reference; its thickness of 200 Å is well-beyond the photoemission probing depth (IMFP $\lambda_i = 15.7$ Å). Basically, the spectrum $M(E_B)$ of the nano-structure to analyse (black circles) should be measured as far as possible in energy including the elastic peak $S(E_B)$ (grey continuous line) and only its own background signal $B(E_B)$ (continuous blue line) to avoid any interference with other core levels. This signal $M(E_B)$ is first corrected by a polynomial interpolation $P(E_B)$ (up to degree 4; dotted grey line) of the background on the low energy side of the elastic peak to get $M^*(E_B) = M(E_B) - P(E_B)$. If available as in the shown example, the same treatment is applied to the reference spectrum $M_r(E_B)$ (red line) of known concentration profile, usually a bulk material. Through a parabolic fit of both maxima over a small window of energy, the binding energy scales ared internally reset, if necessary (*e.g.* to correct from slight charge effects), to have peak maxima at the same position on both $M^*(E)$ and $M_r^*(E)$. The user (i) can choose from a list the kernel of loss $\lambda_i K(T)$ that best describes the matrix at hand for both the actual and reference samples [4, 50, 51] (in the present example, the 3-parameters IESCS suitable for transition/coinage metals (Eq. 3) as the analysed losses are those of Ag 3d core level in Ag itself) or enters its characteristic B, C, D parameters or gives the IESCS itself, (ii) provides estimates of the IMFPs in both samples (see Sect. 4.3) and the emission angle α and (iii) finally selects morphologies (Fig. 8) and concentration profiles of both samples. Morphological parameters are then manually varied until the intrinsic spectrum $S^*(E_B)$, calculated from Eq. 15 or Eq. 16 depending on the selected framework, is as close as possible to the zero line far below the elastic peak. If a reference spectrum is included in the analysis, its $S_r^*(E_B)$ is further subtracted, not only to help visualizing the agreement (green line), but also to determine the relative concentration c/c_r in both samples from their corresponding total integrated intensities P_1 and $P_{1,r}$ (Eq. 17). This parameter c/c_r, which is somehow based on a comparison of absolute intensities, should be in principle close to one; it helps to constraint parameter values such as the coverage for particles. The convolution integrals in Eqs. 15-16, which are well-behaved due to the general behaviour of $\lambda_i K(T)$, are easily handled by fast Fourier transform on a preset number of points [4, 114, 115]. Moreover, for all the chosen profiles, the integrals in P_1 and $P(s)$ (Eq. 17) are analytical [4, 114, 115] leading to negligible calculation time. Thus, IBA can be performed interactively. Two figures of merits χ^2, ϵ_o over the $i = 1, \ldots, N$ experimental points help quantifying the agreement within counting noise defined as $\sigma(E_{B,i}) = \kappa\sqrt{M(E_{B,i})}$ ($\kappa > 0$; green dotted line):

$$\chi^2 = \frac{1}{N}\sum_{i=0}^{N}\frac{M_i^* - B_i^* - P1S_i^*}{\sigma_i^2} \quad (18)$$

$$\epsilon_o = \frac{1}{N}\sum_{i=0}^{N}\Theta_H[\sigma_i - |M_i^* - B_i^* - P1S_i^*|] \quad (19)$$

where $\Theta_H(x)$ is the Heaviside function. ϵ_o corresponds to the fraction of overlapping points which should be as large as possible. Based on one or the other factor, an automated search of the best parameters within a portion of phase space obeying the constraint $|c/c_r - 1| \leq \Delta_c$, can be launched to yield to a final analysis of reliance matrix (see Fig. 9). To help the user, the profile $f(z)$ is replotted in live. All treated spectra $M(E_B), B(E_B), S(E_B), P(E_B), \sigma(E_B), \lambda_i K(T)$ and their reference counterparts are available to the user and are plotted (Fig. 9). In passing, the shown example of Fig. 9 yields to $\Delta z_0 \simeq 30$ Å-high islands covering $f = 70$ % of the surface for a mass thickness of 14.4 Å in perfect agreement with the calibrated one [118]. More than this interesting morphological outcomes, this example of IBA sheds light on differences between elastics peaks of the sample and of the bulk Ag reference (green line); they correspond to a slight Ag oxide contribution as O_2 was introduced during particle growth leading, at such a thickness, to a percolated but not yet continuous film ($f = 70$ %) [118].

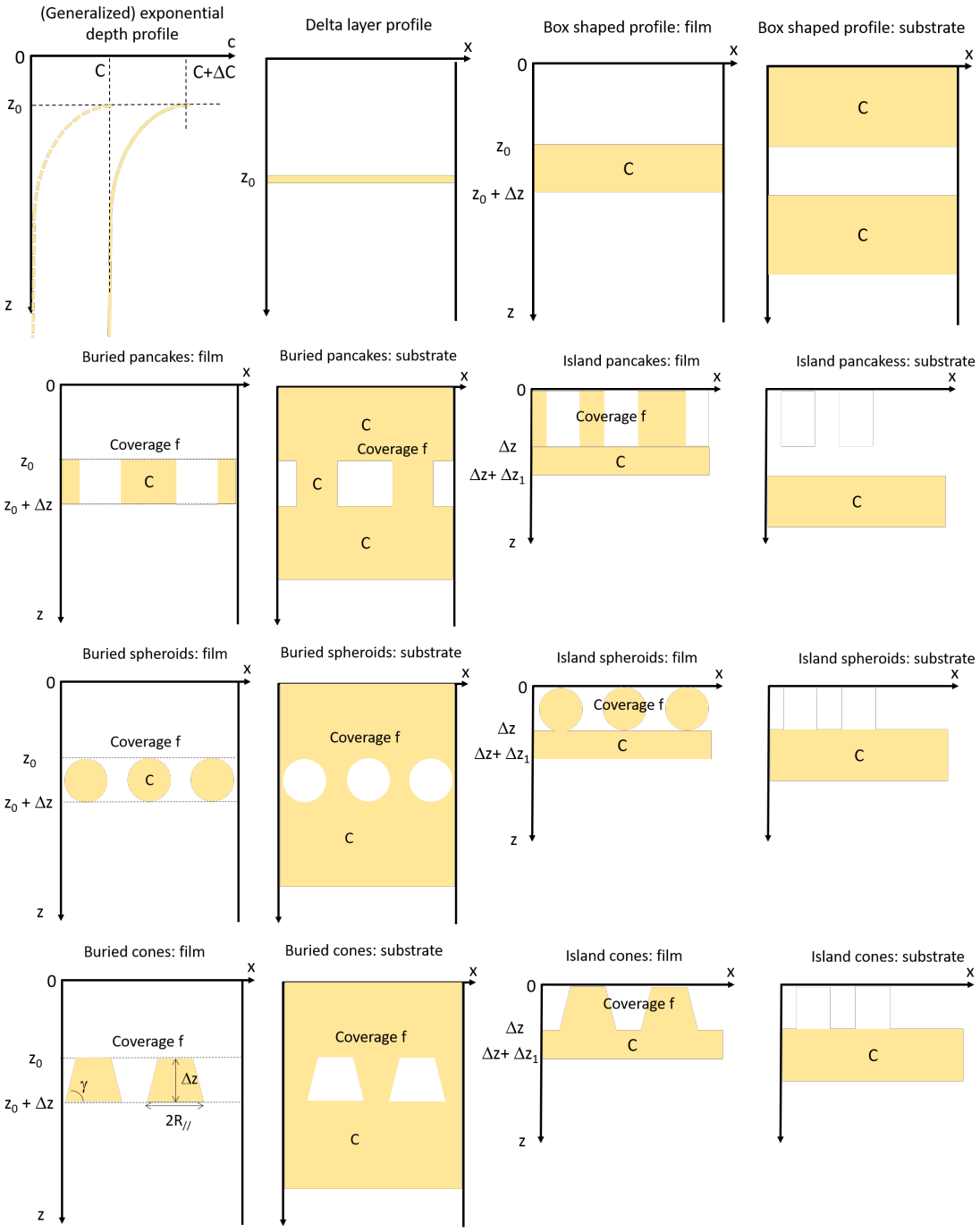

Figure 8: Morphologies corresponding to depth profiles $f(z)$ available in *I4P* for inelastic background analysis. Some morphologies are associated to their counterpart in negative. The coloured area corresponds to the material which photoemission background is analysed. f is the fraction of the surface covered by nanoparticles as seen from above and c the atomic concentration in the coloured area. Some morphologies are redundant (*e.g.* pancakes with $f = 1$ correspond to a a box shape).

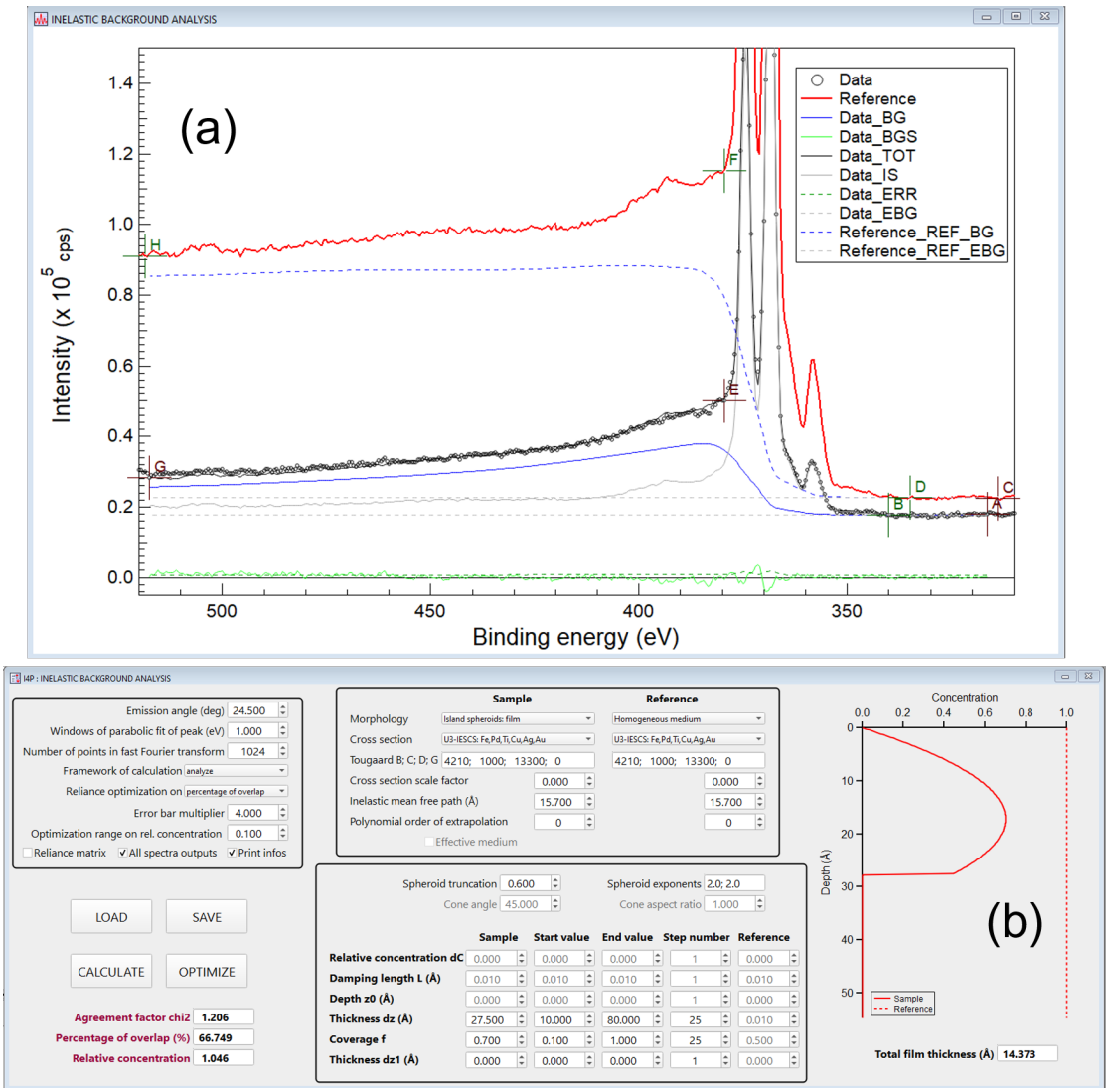

Figure 9: Example of inelastic background analysis of Ag islands on SiO_2/Si with truncated spheres partially covering the surface. (a) Interactive graph with all spectra (see text for definitions): $M(E_B)$ (black circles), $S(E_B)$ (grey continuous line), $B(E_B)$ (continuous blue line), $P(E_B)$ (dotted grey line), $M_r(E_B)$ (red line), $B_r(E_B)$ (blue dotted line), $M^*(E_B) - B(E_B)^* - P1S^*(E_B)$ (green line), $\sigma(E_B)$ (green dotted line). Cursor pairs $(A, B)/(C, D)$ are used to define the background polynomial extrapolations, $(B, E)/(D, F)$ to estimate elastic peak areas and $(A, G)/(C, H)$ to restrict the analysed range of energy. (b) Interactive panel for setting simulation parameters, morphological parameters and visualising the concentration profile $f(z)$, the agreement factors χ^2, ϵ_o and the relative concentration c/c_r compared to reference (see text for explanations).

6. Peak fitting

Peak fitting is at the heart of photoemission analysis. The idea is to decompose the initial spectrum $I(E_B)$ in a sum of N components (or peaks) $P_k(E_B)$ and an inelastic background $B(E_B)$. Within reasonable hypothesis regarding the studied sample, each component corresponds to a different oxydo-reduction state of the probed atom, or more generally to different chemical environments. Compared to this first sight initial state picture, final state effects can lead to more entangled spectral features [25, 119]. The atom after photoionisation may be left in an excited state by the outgoing electron leading to specific shake-up satellite peaks. In the case of atoms with unpaired electrons in the valence states, the exchange interaction with the unpaired electrons created by the photoionisation process in the core level leads to a number of final states. This multiplet splitting gives rise to broadened photoemission peaks when unresolved or to more distinct satellites features. Thus fitting is not an easy task as an inexperienced user can face many pitfalls and ends in wrong results if basic physical inputs and constraints are not properly accounted for (see review Refs. [19, 21, 23, 24]). In a complementary way to stand-alone existing tools [27, 28] or those related to apparatus suppliers, the *I4P* fit menu offers a great flexibility in handling background, peak line shape, constraints, peak broadening and source satellites. Further development by the user is possible as the source code is freely available.

6.1. Fit environment

The fit environment consists in (i) a graph panel where data, fit, peaks, background and residues are displayed and (ii) a peak manager panel (Fig. 10). At the spectrum loading stage, the error bars $\sigma(E_B)$ on $I(E_B)$ required in the fit process can be defined in different ways: (i) counting statistics $\sigma(E_B) = \sqrt{I(E_B)}$, (ii) proportional to the intensity $\sigma(E_B) = \kappa\sigma(E_B)$ with $\kappa > 0$ a user-defined value, (iii) constant $\sigma(E_B) = \kappa$ and (iv) via deviation from a polynomial interpolation over a moving window. The last method turns out to be the most accurate in estimating noise. Each peak, which can be (de)activated at will for fit, corresponds to a page in a spreadsheet in which the user can browse easily from peak to peak. All parameters describing each peak are entered in table. Fit template can be saved and reloaded. Batch fit is possible in the case of a series of spectra; final outputs allow for an easy plot of the fit parameter evolutions.

6.2. Background and resolution

The inelastic background is accounted for during the fit and does not need to be subtracted before. This so-called "active" background fitting was shown to lead to more consistent results [22, 45, 120] as background removal is prone to arbitrariness in particular for the choice of end points as in the case of Shirley one (Eq. 1). Aside an optional polynomial up to order three $B_P(E_B)$, all integral backgrounds $B_I(E_B)$ previously detailed in Sect. 3.3 (Eqs. 1-4) can be selected and their parameters fitted. $B_I(E_B)$ is obtained from the peak sum $\sum_k P_k(E_B)$; it is calculated numerically by integration (Eqs. 1-2) or by convolution in reciprocal space and a self-consistent loop (Eqs. 3-4). Alternatively, each peak can be associated to its own background the parameters of which may differ from component to component; this option is of interest when dealing with core levels of elements distributed quite differently in depth. A global instrumental broadening can be applied to the whole theoretical spectrum $B_P(E_B) + B_I(E_B) + \sum_k P_k(E_B)$ through convolution with various functions (gaussian, slit, triangle). Similarly, each peak $P_k(E_B)$ can be broadened individually via a convolution with a gaussian; aside instrument contribution, this broadening is usually assigned to distribution of chemical environments, fluctuation of surface potential or band bending. A general correction by a $R_F(E_K) = 1/E_K^{\alpha}$ (α fitting constant) can also be included in the fit. A special attention has historically been paid to the treatment of source satellites of Al/Mg-Kα anodes by convolution (or simple summation) applied to $\sum_k P_k(E_B)$ using tabulated values of relative positions, widths and intensities of emission lines [41, 42]. As for background, their removal by deconvolution prior to fit (Sect. 3.2) may distort the spectrum line shape in particular when the energy range is restricted. Satellites complicates the fit of low intensity features, in particular for core levels with large spin-orbit splitting; they should be accounted for properly. As the presence of K$\alpha_{1,2}$ components in the main peak worsens the overall resolution, a monochromated x-ray beam is always advised. Nevertheless, by treating each photo-peak by the contribution from the Kα_1 line plus all its satellites K$\alpha_{2,3,4,5,6} - K\beta$, convincing results can be achieved (see below Sect. 6.5.2 and 6.5.4). Of course, the approach can be extended to other anodes provided that their emission spectra are well characterized.

6.3. Peak line shapes

Each peak $P_k(E_B)$ is described by its own line shape selected in a library of 17 different profiles: (1) lorentzian, (2) gaussian, (3) Voigt *i.e.* convolution of gaussian and lorentzian, (4) pseudo-Voigt or weighted sum of gaussian and lorentzian, (5) product lorentzian-gaussian, (6) oscillator, (7) Doniach-Sunjic [121], (8) generalized Doniach-Sunjic, (9) Mahan [122], (10) post-collision interaction [123]: (11) asymmetric Voigt, (12) asymmetric pseudo-Voigt [124], (13) step functions, (14) Fano, (15) plasmon [2], (16) band bending with lorentzian profile [125], (17) Gadzuk-Sunjic [126]. Their definitions are given in the *I4P* manual and in supporting information. Asymmetric profiles [(7),(8),(9)(10)(11)(12)] are mostly used to describe the electron-hole excitations in metals. Plasmon replicas [(15)], described by their Poisson (extrinsic losses) or arithmetic (intrinsic losses) statistics as described in Ref. [2], can be linked to any core level peak via internal constraints. Peak broadening through parabolic band-bending in a space charge layer [(16)] [125] can also

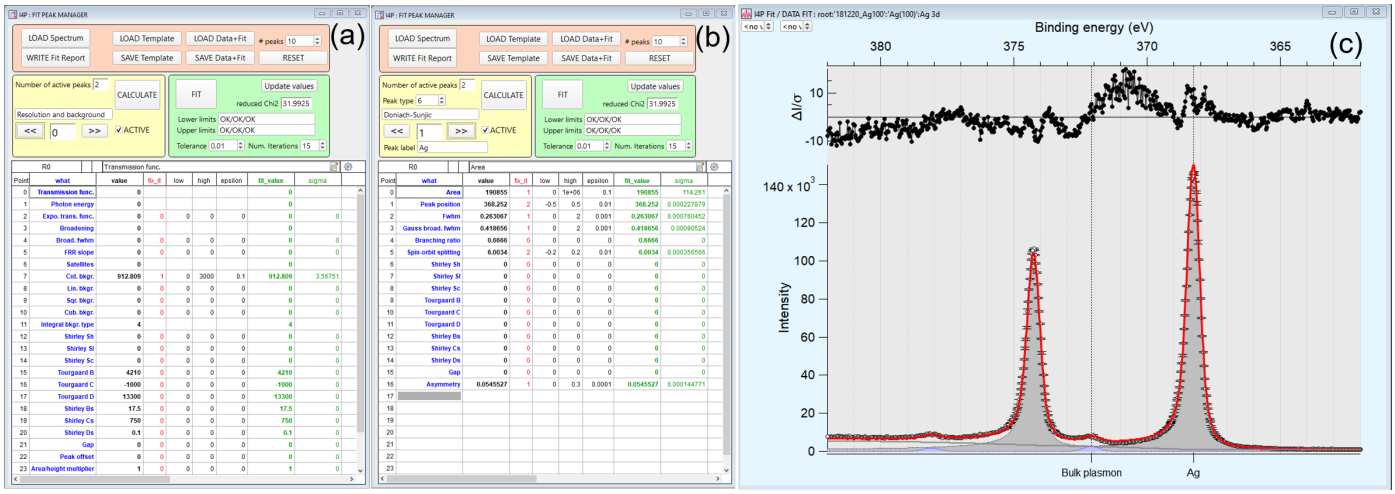

Figure 10: *I4P* panels for fit: parameters of (a) background and resolution and of (b) peaks associated to (c) fit graph (data: dot with error bars; fit: red line; background: grey line; symbols on top: residuals normalised to error bars). The columns in the table (Figs. a-b) correspond, from left to right, to: (i) parameter name, (ii) parameter value, (iii) code to define constraints [37], (iv) limits, (v) fitted values and its error bars. The example corresponds to the analysis of Ag 3d core level of a clean Ag(100) single crystals recorded with a Al-Kα monochromated x-ray source. Only a spin-orbit split Doniach-Sunjic asymmetric line shape was used with the theoretical branching ratio of 2/3. The background is described by a 3-parameters Tougaard function with tabulated parameters. A bulk plasmon shifted by 3.8 eV is added to the fit.

be accounted for. At last, the step functions are specific for the analysis of Fermi edge or of the secondary electron cut off; they include specific treatments of broadening (*e.g.* Fermi statistics) and of background for an accurate calibration of $E_B = 0$ and of the material work function. Each peak $P_k(E_B)$ (except step functions) is characterized by a central value $E_{B,0}$, a scale factor A and a width W which, in most cases, correspond to position, area and FWHM, respectively. These parameters are used to discuss chemistry and physics of the system: (i) chemical shift, (ii) quantification, (iii) photo-hole lifetime folded with the width of the x-ray emission line.

As said before, each peak can be linked to its own background and broadened by gaussian convolution to account for instrument and distribution of chemical states or fluctuations of surface potential. By default, the peak is assumed to be spin-orbit split with the same broadening for the two components, but with an adjustable splitting and branching ratio. The latter should be set at $1/2, 2/3, 3/4$ to account for the degeneracy due to the $L-S$ coupling of p, d and f levels. Of course, for s level, the second component should be set to zero.

6.4. Fit method and constraints

Fit is performed with the non-linear χ^2 least-squares Levenberg-Marquardt algorithm [44] with preset constraints (see below). It is performed over the full data range or between binding energies indicated by cursors. Beyond visual inspection, fit quality can be assessed from agreement factors defined as:

$$\begin{aligned}
\chi^2 &= \frac{1}{N-n}\sum_{i=1}^{N}\left[\frac{y_i^t - y_i^e}{\sigma_i}\right]^2; \\
R_b &= \frac{\sum_{i=1}^{N}|y_i^t - y_i^e|}{\sum_{i=1}^{N}|y_i^e|}; \\
R_b^e &= \sqrt{\frac{N-n}{\sum_{i=1}^{N}(y_i^e/\sigma_i)^2}}; \\
A_b &= \frac{1}{2}\frac{\sum_{i=1}^{N}[y_{i+1}^t - y_{i+1}^e - (y_i^t - y_i^e)]}{\sum_{i=1}^{N}(y_i^t - y_i^e)^2}.
\end{aligned} \tag{20}$$

y_i^e, y_i^t, σ_i with $i = 1, \ldots, N$ are the experimental data points, the calculated points and the input error bars, respectively. n is the number of free parameters in the fit. Reliance parameters χ^2, R_B, R_B^e, the error bars in parameters and the matrix of correlation coefficients as obtained from the curvature of χ^2 at minimum are given in the fit report. A satisfactory fit is characterised by χ^2 close to one, R_B close to R_B^e and Abbe value A_b close to one (when close 2 or 0, it means anti-correlated or correlated residuals). The report includes also a extra informations on all peaks such as actual areas, positions of maximum and FWHMs calculated numerically on the used binding energy range; indeed, at the opposite to for instance a gaussian peak, only a scale factor and a characteristic broadening are fitted for some asymmetric peaks and not the actual peak area or FWHM.

Parameters can be fixed or fitted between soft limits that are defined in absolute or relative values compared to the parameter at hand. Link between peak parameters of the same kind (e.g. area, position, FWHM, spin-orbit

splitting, etc...) can be configured in different ways: (i) $p_1 - \Delta p \leq p_2 \leq p_1 - \Delta p$, (ii) $p_2 = p_1 + \Delta p$, (iii) $p_2 = p_1 + p_3$, (iv) $p_2 = p_1 \Delta p$, (v) $p_2 = p_1 p_3$, where p_1, p_2, p_3 are the values of the 3 linked peaks and Δp is a constant. For instance, constraints (ii) with $\Delta p = 0$ ensures parameter equality. But this can be achieved with constraint (i) within a small Δp range to give a bit of flexibility; this is useful when enforcing chemical shifts between different oxido-reduction states as found in literature and databases [20]. Relative peak intensities can be fixed with constraint (iv) as in the case of C 1s level of an organic molecule with known chemical formula (see Sect. 6.5.1). At last, one can enforce normalized IESCS as expected from theory [51]; in other words, the B-parameter in Eq. 3 during fit is analytically linked to C through:

$$\int \lambda_i K(T) dT = 1. \tag{21}$$

6.5. Example of fits

The following examples illustrate the capabilities of *I4P* fit menu in terms of constraints, satellite handling or choice of background. Further examples can be found in Refs. [111, 113, 118, 127].

6.5.1. The PET polymer

The C 1s region of a sample of polyethylene terephthalate (PET) polymer has been recorded on a SPECS Phoibos analyser equipped with a delay line detector and a monochromated Al-Kα source. The emission angle was set at $\alpha = 35°$ and the sample prepared by gently scratching the surface with a razor blade. Charge compensation through a flood gun was adjusted to have the stablest and sharpest peak. The fit (Fig. 11) of the four inequivalent environments of C atoms has been performed with Voigt peaks having the same lorentzian (0.15 eV) and slightly different gaussian broadenings (0.9-1.1 eV). Their relative areas have been fixed according to the chemical formula: $A(C_2)/A(C_1) = 0.5$, $A(C_3)/A(C_1) = 0.5$, $A(C_4)/A(C_1) = 0.5$. Two Voigt shake-up satellites due to $\pi - \pi^*$ transitions have been added in the form of gaussian peaks. The inelastic background was not fitted but fixed at Tougaard values characteristic of a polymer [51]: $A = 434$ eV^2, $B = 551$ eV^2, $C = 436$ eV^2. All peak binding energies were freely fitted leading to chemical shifts relative to C_1 of $\Delta E_B(C_2 - C_1) = 1.64$ eV, $\Delta E_B(C_3 - C_1) = 4.00$ eV, $\Delta E_B(C_4 - C_1) = 0.24$ eV. The fit is good as demonstrated by the agreement factors $\chi^2 = 0.9$, $R_B = 0.025$ (for $R_b^e = 0.04$) and $A_B = 0.35$ and the visual inspection of residuals (Fig. 11).

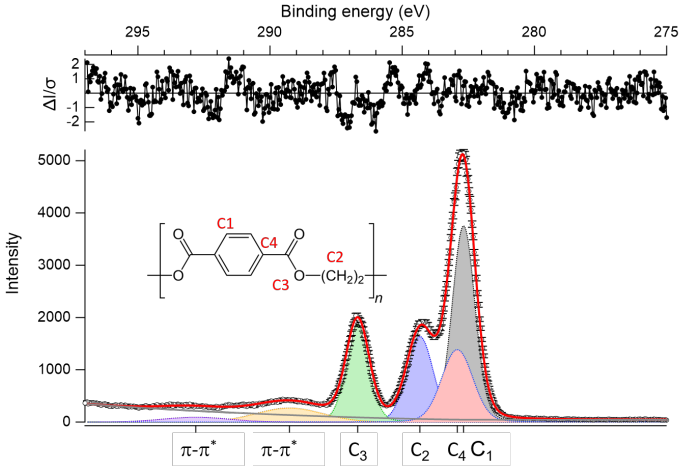

Figure 11: Fit of the C 1s region of PET: (circles with error bars) data; (red line) total fit; (grey line) background; (coloured peaks) different C environments as indicated in the chemical formula; (top) residuals normalised by error bars. Error bars on data are defined by the deviation from a polynomial interpolation of data over a moving window.

6.5.2. Titanium dioxide

Fig. 12 shows the fit of the Ti 2p core level of a single crystal TiO_2(110) surface. The spectrum was acquired at normal emission with an Omicron EA125 apparatus and an unmonochromated Mg-Kα source. The sample was prepared by cycles of sputtering-annealing [128] and dosed with O_2 to minimize the Ti^{3+} contribution from defects. The spin-orbit split 2p peak was described by two Voigt profiles having the expected area ratio of 1/2 but different widths. Indeed, the broadenings of the 1/2 and 3/2 components differ due to the presence of many unresolved final states underneath the 1/2 peak [129]. Two shake-up satellites with the same splitting and relative intensities as the Ti 2p 1/2-3/2 main lines have been added. All satellites of the Mg-Kα source [41, 42] have been included while fitting. Two different types of background which parameters have been fitted were tested: (i) 2-parameters normalized Tougaard (Eq. 3) or (ii) Shirley (Eq. 1). A slightly better fit, in particular in between the two 2p components, could be achieved with the Shirley background ($\chi^2 = 0.5$ vs $\chi^2 = 1.3$). Note that, for both backgrounds, only one parameter is fitted (S_h for Shirley and C for Tougaard). Nevertheless, the commonly used Shirley background that assumes a simple proportionality between background and the integral of intrinsic peak at higher kinetic energy has no physical foundation! J. Vegh [54, 55] demonstrated that it could be theoretically associated to a fictitious IESCS $\lambda_i K(T)$ as given by Eq. 4. The comparison to the one found in the case of Tougaard background is shown in the inset of Fig. 12-a. Obviously, they strongly differ but the Tougaard IESCS with a peak centred around 10 eV matches quite well the reflection energy loss spectroscopy (REELS) findings and dielectric modelling of Fuentes *et al.* on TiO_2 [130].

6.5.3. Oxidized silicon

A Si(001) wafer with its native oxide layer was probed by photoemission with the same apparatus as for PET (monochromated Al-Kα source, $\alpha = 35°$, $\psi = 70°$). The sample was outgassed at high temperature under ultra-

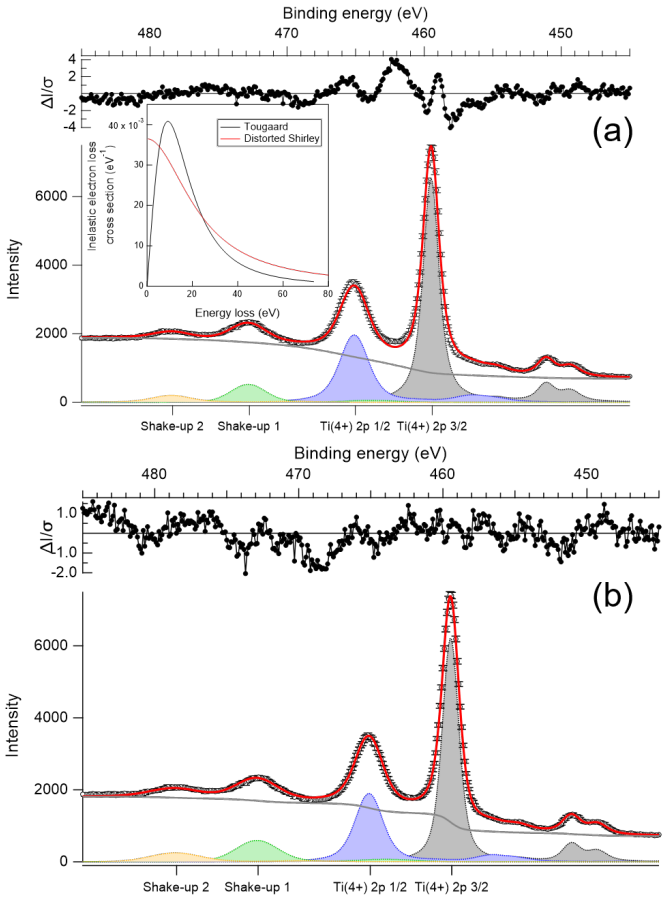

Figure 12: Fit of the Ti 2 p core level of TiO_2 with a (a) Tougaard or (b) Shirley background. Same legend as Fig. 11. The corresponding IESCS are shown in inset of Fig. a.

high vacuum; it was free of C contamination. The Si 2p core level region was recorded on a wide range of binding energies, including not only $Si^{(0)}$ and $Si^{(4+)}$ components, but also the plasmon loss at $E_B = 117.5$ eV. The fit was performed with two spin-orbit split 2 p Voigt components corresponding to Si and SiO_2; Si suboxides were ignored. Branching ratio was set at 1/2 and the splitting was constrained to be the same for both peaks; the found value of 0.62 eV is very close to literature [20]. The background was accounted for with a 3-parameters IESCS normalized to one (Eq. 21); as expected, the values obtained for C, D are close to those tabulated by Tougaard for Si [51]. The fit is not perfect over such a large range ($\chi^2 = 5.6$, $R_B = 0.07$ for $R_B^e = 0.04$) because of the description of the plasmon loss with the used IESCS. From the ratio of peak areas (68 %/32 %) of $Si^{(0)}/Si^{(4+)}$, an oxide thickness of 14.7 Å can be estimated from Eq. 9 using the *I4P* tools for quantification (Sect. 5.1) and for mean free path calculations (Sect. 4.3). To do so, elastic scattering is taken into account through bulk and effective film EALs [9, 102]: $\lambda_{ss}^{eb} = 38.8$ Å, $\lambda_{sf}^{ef} = 29.7$ Å, $\lambda_{ff}^{eb} = 41.3$ Å and $\lambda_{ff}^{ef} = 29.7$ Å derived from (i) IMFPs $\lambda_s = 29.6$ Å, $\lambda_f = 30.9$ Å and albedos $\omega_s = 0.115$, $\omega_f = 0.058$ [(s) : Si substrate, (f): SiO_2 film], (ii) the apparatus geometry ($\alpha = 35°$, $\psi = 70°$, $\theta = 35°$) and (iii) the asymmetry factor $\beta = 1.026$ of Si 2p [35]. IMFP and albedo (and therefore TRMFP) were obtained from the JPT predictive formula [6] and database of Ref. [86], respectively. No correction from $R_F(E_K)$ or PICS are necessary since both substrate and film features come from the same core level; only the bulk densities are required ($n_s = 0.0830$ and $n_f = 0.0441$ mol.cm^{-3}). On the one hand, if IMFPs are used, a slight larger thickness (15.6 Å) is found. On the other hand, the SEP correction leads to a much smaller thickness value of (12.1 Å) in close agreement with medium-energy ion scattering measurements ($\sim$ 13 Å) for the oxidised part of the wafer [131]. This example of oxidised Si points out uncertainties related to modelling (IMFPs vs EALs, account of SEPs). But, as a rule of thumb, the intrinsic uncertainties related to IMFPs and EALs from a given datebase (which are below $\sim$ 10 % for the JPT predictive formula) are of second order as these parameters come into play somehow in the form of ratios. Note that this peculiar example corresponds to a model system for which interfaces are flat and clean without PICS and $R_F(E_K)$ corrections between core levels.

6.5.4. Oxidized silver

Films of Ag were grown by magnetron sputtering on Si wafer using a mixture of Ar(60 %)/O_2(40 %) (see Ref. [118] for all details). Atomic O due to the dissociation of the O_2 molecules in the plasma led to the partial oxidation of Ag. The phenomenon was followed as a function of film thickness by Ag 3d photoemission under unmonochromated Al-Kα excitation with a Phoibos 100 analyser equipped with channeltron detectors. As all Ag (sub)oxides poorly differ

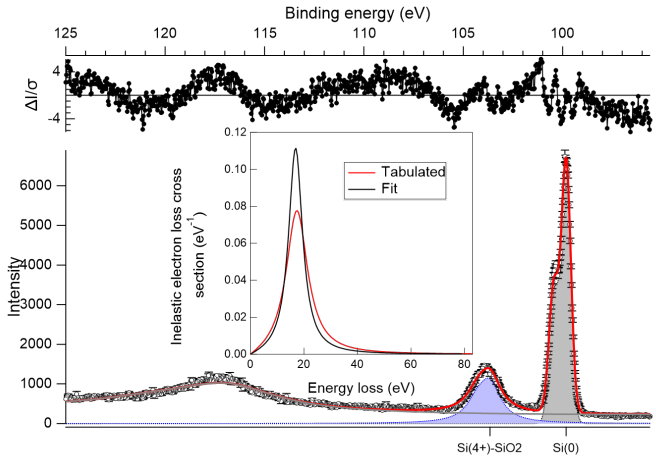

Figure 13: Fit of the Si 2p region of an oxidised Si wafer. Same legend as Fig. 11. The inset shows the fitted and tabulated IESCS.

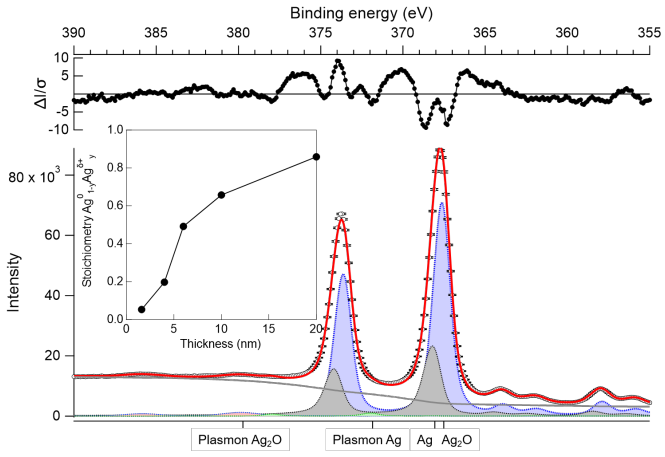

Figure 14: Fit of the Ag 3d region of a 20 nm thick film grown by magnetron sputtering under Ar(60 %)/O_2(40 %) mixture. Same legend as Fig. 11. The inset shows the evolution of film stoichiometry with thickness.

in terms of chemical shift compared to the metal [118], the Ag 3d core level was fitted with only two Voigt components corresponding to $Ag^{(0)}$ and $Ag^{(\delta+)}$ ($\Delta E_B = -0.5$ eV). Note the unusual negative core level shift between oxidised and metallic silver which is due to complex final state effects. Aside these two main contributions, two minor plasmon loss peaks in Ag ($\Delta E_B = +3.8$ eV) and AgO_x ($\Delta E_B = +11.7$ eV) had to be introduced. All 3 d core level peaks have the same 2/3 theoretical branching ratio and the same energy splitting. They were accompanied by all satellites of the Al anode. The lorentzian width of Ag 3d peaks was constrained to be at least equal to that of $K\alpha_1$ line of the source (0.58 eV). A Doniach-Sunjic profile [121] was used only for the metallic component; its asymmetry was obtained from a reference spectrum of pure Ag ($\alpha = 0.05$). The inelastic background was described with the 3-parameter Tougaard IESCS characteristic of Ag [51]. The fit parameters obtained for the thickest film (20 nm; Fig. 14) were then propagated to thinner ones to get only the relative ratio of metallic and oxidised Ag components without fitting other parameters. No other specific correction was required to extract the effective film stoichiometry $Ag^{(0)}_{1-y}Ag^{(\delta+)}_{y}$ as shown in the inset of Fig. 14. Of course, as seen already in the y evolution with thickness, an in-depth gradient of oxidation is present with more metallic Ag close to the interface with the substrate. Such a finding was related to a competition between oxidation and metal aggregation and substrate reactivity [118]. Thus, the evolution of y does no reflect the actual profile of composition as it is derived from an homogeneous material hypothesis and the photoemission signal is integrated over the probing depth.

7. Software distribution and prospects

The *I4P* suite is freely available from internet [37] under the GNU Public License agreement. It comes with an up-to-date and detailed user manual including all useful references to the literature at the heart of *I4P*. All the source code is fully commented and easily editable. In particular, aside clickable menus, most of the previously described *I4P* functionalities are associated to function calls (*e.g.* peak area after background subtraction, EALs, etc...), the syntax of which are carefully detailed; in such a way, the user can further developed its own scripting modules. *I4P* comes with extended databases of PICS in the form of external *csv* files (digitized versions of PICS databases from Refs. [71–75]) or internally coded in the *I4P* module files. Foreseen developments will deal with handling results from 2D detector and imaging. Although versatile and widespread in the research community, the *Igor Pro* software [38] *per se* is not free of charge. Thus, an equivalent implementation under *Python* environment is under consideration.

8. Conclusion

A stand-alone and easy-to-use package, called *I4P*, has been developed for photoemission analysis under the *Igor Pro* scripting language. While being complementary to all available tools, it covers all basic data treatments, but offers improved or new functionalities in terms of quantification, peak fitting and response function calibration. It is associated to up-to-date databases of binding energies, photo-ionisation cross sections, inelastic mean free paths, effective attenuation lengths for both low and high energy sources. The main *I4P* strength is to gather in a open and freely available package all the tools required by the photemission spectroscopist while offering him the capabilities to develop her/his own treatments.

Acknowledgements

The author would like to thank all his INSP colleagues (G. Cabailh, S. Guilet, A. Levy) for their suggestions and supports during the development of *I4P*.

References

[1] S. Hofmann, Auger and X-ray photoelectron spectroscopy in material science, Springer, 2013.
[2] S. Hüfner, Photoelectron spectroscopy: principles and applications, Springer, 1995.
[3] F. A. Stevie, C. L. Donley, Introduction to x-ray photoelectron spectroscopy, J. Vac. Sci. Technol. A 38 (2020) 063204.
[4] S. Tougaard, Energy loss in XPS: Fundamental processes and applications for quantification, non-destructive depth profiling and 3D imaging, J. Electron Spectrosc. Relat. Phenom. 178-179 (2010) 128 – 153.
[5] S. Tougaard, Practical guide to the use of backgrounds in quantitative XPS, J. Vac. Sci. Technol. A 39 (2021) 011–201, 011201.
[6] A. Jablonski, S. Tanuma, C. J. Powell, Calculations of electron inelastic mean free paths (IMFPs). XIV. Calculated IMFPs for LiF and Si_3N_4 and development of an improved predictive IMFP formula, Surf. Interface Anal. 55 (2023) 609–637.
[7] V. I. Nefedov, Photoelectron elastic scattering effects in XPS, J. Electron Spectrosc. 100 (1999) 1–15.
[8] W. S. M. Werner, Electron transport in solids for quantitative surface analysis, Surf. Interface Anal. 31 (2001) 141–176.
[9] A. Jablonski, C. J. Powell, The electron attenuation length revisited, Surf. Sci. Rep. 47 (2002) 33–91.
[10] C. J. Powell, A. Jablonski, Progress in quantitative surface analysis by X-ray photoelectron spectroscopy: Current status and perspectives, J. Electron Spectrosc. 178-179 (2010) 331–346.
[11] A. Jablonski, C. J. Powell, Effective attenuation lengths for different quantitative applications of x-ray photoelectron spectroscopy, J. Phys. Chem. Ref. Data 49 (2020) 033102.
[12] M. B. Trzhaskovskaya, V. G. Yarzhemsky, Dirac-Fock photoionization parameters for HAXPES applications, Atom. Data Nucl. Data 119 (2018) 99–174.
[13] M. B. Trzhaskovskaya, V. G. Yarzhemsky, Dirac-Fock photoionization parameters for HAXPES applications, Part II: Inner atomic shells, Atom. Data Nucl. Data 129-130 (2019) 101280.
[14] A. G. Shard, Practical guides for x-ray photoelectron spectroscopy: Quantitative XPS, J. Vac. Sci. Technol., A 38 (2020) 041201.
[15] F. A. Stevie, R. Garcia, J. Shallenberger, J. G. Newman, C. L. Donley, Sample handling, preparation and mounting for XPS and other surface analytical techniques, J. Vac. Sci. Technol. A 38 (2020) 063202.
[16] G. Greczynski, L. Hultman, A step-by-step guide to perform x-ray photoelectron spectroscopy, J. Appl. Phys. 132 (2022) 011101.
[17] J. Wolstenholme, Procedure which allows the performance and calibration of an XPS instrument to be checked rapidly and frequently, J. Vac. Sci. Technol. A 38 (2020) 043206.
[18] S. Guilet, L. Bataillou, O. Kerivel, R. Lazzari, Determination of the intensity/energy response function of an hemispherical photoelectron analyser based on Tougaard background, J. Electron Spectrosc. 258 (2022) 147225.
[19] G. H. Major, T. G. Avval, B. Moeini, G. Pinto, D. Shah, V. Jain, V. Carver, W. Skinner, T. R. Gengenbach, C. D. Easton, A. Herrera-Gomez, T. S. Nunney, D. R. Baer, M. R. Linford, Assessment of the frequency and nature of erroneous x-ray photoelectron spectroscopy analyses in the scientific literature, J. Vac. Sci. Technol. A 38 (2020) 061204.
[20] NIST X-ray photoelectron spectroscopy database, https://srdata.nist.gov/xps/Default.aspx (2012).
[21] P. M. A. Sherwood, The use and misuse of curve fitting in the analysis of core x-ray photoelectron spectroscopic data, Surf. Interface Anal. 51 (2019) 589–610.
[22] A. Herrera-Gomez, Uncertainties in photoemission peak fitting accounting for the covariance with background parameters, J. Vac. Sci. Technol. A 38 (2020) 033211.
[23] G. H. Major, N. Fairley, P. M. A. Sherwood, M. R. Linford, J. Terry, V. Fernandez, K. Artyushkova, Practical guide for curve fitting in x-ray photoelectron spectroscopy, J. Vac. Sci. Technol. A 38 (2020) 061203.
[24] G. H. Major, V. Fernandez, N. Fairley, E. F. Smith, M. R. Linford, Guide to XPS data analysis: Applying appropriate constraints to synthetic peaks in XPS peak fitting, J. Vac. Sci. Technol. A 40 (2022) 063201.
[25] V. Crist, The XPS library, https://xpslibrary.com/.
[26] Harwellxps, https://www.harwellxps.guru/knowledgebase/software/.
[27] N. Fairley, CasaXPS: Processing Software for XPS, AES, SIMS and More, //http://www.casaxps.com/.
[28] R. Hesse, UniFit for Windows: The Art of Peak Fit, https://www.unifit-software.de/.
[29] S. Tougaard, QUASES: software packages to characterize surface nano-structures by analysis of electron spectra, http://www.quases.com/.
[30] C. Powell, NIST Database for the Simulation of Electron Spectra for Surface Analysis (SESSA), https://www.nist.gov/srd/nist-standard-reference-database-100.
[31] W. Smekal, W. S. M. Werner, C. J. Powell, Simulation of electron spectra for surface analysis (SESSA): a novel software tool for quantitative auger-electron spectroscopy and x-ray photoelectron spectroscopy, Surf. Interface Anal. 37 (11) (2005) 1059–1067.
[32] C. J. Powell, A. Jablonski, NIST electron inelastic mean free path database, https://www.nist.gov/srd/nist-standard-reference-database-71 (2010).
[33] S. Tougaard, QUASES-IMFP-TPP2M Software, http://www.quases.com/products/quases-imfp-tpp2m/.
[34] J. H. Scofield, Theoretical photoionization cross sections from 1 to 1500 kev., Technical Report UCRL-51326, Lawrence Livermore Laboratory (1973).
[35] J. Yeh, I. Lindau, Atomic subshell photoionization cross sections and asymmetry parameters: $1 \leq z \leq 300$, At. Data Nucl. Data Tables 32 (1985) 1–155.
[36] D. J. H. Cant, B. F. Spencer, W. R. Flavell, A. G. Shard, Quantification of hard x-ray photoelectron spectroscopy: Calculating relative sensitivity factors for 1.5- to 10-keV photons in any instrument geometry, Surf. Interface Anal. 54 (2022) 442–454.
[37] R. Lazzari, *Igor Pro Paris Photoemission Package* can be downloaded with a user guide from: https://w3.insp.upmc.fr/en/research/research-teams/low-dimensional-oxides/low-dimensional-oxides-facilities/low-dimensional-oxides/.
[38] https://www.wavemetrics.com/, Igor Pro from WaveMetrics.
[39] W. A. Dench, L. B. Hazell, M. P. Seah, VAMAS surface chemical analysis standard data transfer format with skeleton decoding programs, Surf. Interface Anal. 13 (1988) 63–122.
[40] C. D. Wagner, W. M. Riggs, L. E. Davis, J. F. Moulder, G. E. Muilenberg, Handbook of X-Ray Photoelectron spectroscopy, Perkin-Elmer, Eden Prairie, 1979.
[41] C. Klauber, Refinement of magnesium and aluminium Kα x-ray source functions, Surf. Interface Anal. 20 (8) (1993) 703–715.
[42] M. O. Krause, J. G. Ferreira, K X-ray emission spectra of Mg and Al, J. Phys. B: At. Mol. Phys. 8 (12) (1975) 2007.
[43] Manual of HIS13 source from Focus GmbH.
[44] W. H. Press, S. A. Teukolsky, W. T. Vetterling, B. P. Flannery, Numerical Recipes in Fortran, Cambridge University Press, 1992.
[45] A. Herrera-Gomez, M. Bravo-Sanchez, O. Ceballos-Sanchez, M. O. Vazquez-Lepe, Practical methods for background sub-

traction in photoemission spectra, Surf. Interface Anal. 46 (2014) 897–905.
[46] M. H. Engelhard, D. R. Baer, A. Herrera-Gomez, P. M. A. Sherwood, Introductory guide to backgrounds in XPS spectra and their impact on determining peak intensities, J. Vac. Sci. Technol., A 38 (2020) 063203.
[47] D. Shirley, High-resolution X-ray photoemission spectrum of valence bands of gold, Phys. Rev. B 5 (1972) 4709–4714.
[48] A. Proctor, P. M. A. Sherwood, Data analysis techniques in x-ray photoelectron spectroscopy, Anal. Chem. 54 (1982) 13–19.
[49] A. Herrera-Gomez, M. Bravo-Sanchez, F. S. Aguirre-Tostado, M. O. Vazquez-Lepe, The slope-background for the near-peak regime of photoemission spectra, J. Electron Spectrosc. Relat. Phenom. 189 (2013) 76 – 80.
[50] S. Tougaard, Quantitative analysis of the inelastic background in surface electron spectroscopy, Surf. Interface Anal. 11 (9) (1988) 453–472.
[51] S. Tougaard, Universality classes of inelastic electron scattering cross-sections, Surf. Interface Anal. 25 (3) (1997) 137–154.
[52] M. P. Seah, Background subtraction: I. General behaviour of Tougaard-style backgrounds in AES and XPS, Surf. Sci. 420 (2) (1999) 285 – 294.
[53] M. P. Seah, I. S. Gilmore, S. J. Spencer, Background subtraction: II. General behaviour of REELS and the Tougaard universal cross section in the removal of backgrounds in AES and XPS, Surf. Sci. 461 (1) (2000) 1 – 15.
[54] J. Végh, The Shirley-equivalent electron inelastic scattering cross-section function, Surf. Sci. 563 (2004) 183–190.
[55] J. Végh, The Shirley background revised, J. Electron Spectrosc. Relat. Phenom. 151 (2006) 159–164.
[56] R. Hesse, P. Streubel, R. Szargan, Improved accuracy of quantitative XPS analysis using predetermined spectrometer transmission functions with UNIFIT 2004, Surf. Interface Anal. 37 (2005) 589–607.
[57] M. P. Seah, G. C. Smith, Quantitative AES and XPS: Determination of the electron spectrometer transmission function and the detector sensitivity energy dependencies for the production of true electron emission spectra in AES and XPS, Surf. Interface Anal. 15 (1990) 751–766.
[58] M. P. Seah, XPS reference procedure for the accurate intensity calibration of electron spectrometers: results of a BCR intercomparison co-sponsored by the VAMAS SCA TWA., Surf. Interface Anal. 20 (1993) 243–266.
[59] M. P. Seah, AES and XPS measurements: reducing the uncertainty and improving the accuracy, Appl. Surf. Sci. 70-71 (1993) 1–8.
[60] D. Alamarguy, D. Aureau, T. Conard, F. Georgi, S. Guilet, S. Hajjar-Garreau, O. Heintz, G. Monier, C. Méthivier, H. Montigaud, S. Soule, O. Renault, R. Lazzari, Intensity-energy response function of Al/Cr-kα x-ray photoemission instruments: an inter-laboratory study, submitted (2024).
[61] A. G. Shard, S. J. Spencer, Intensity calibration for monochromated Al Kα XPS instruments using polyethylene, Surf. Interface Anal. 51 (2019) 618–626.
[62] A. G. Shard, B. P. Reed, Al Kα XPS reference spectra of polyethylene for all instrument geometries, J. Vac. Sci. Technol. A. 38 (2020) 063209.
[63] B. P. Reed, D. J. H. Cant, S. J. Spencer, A. J. Carmona-Carmona, A. Bushell, A. Herrera-Gómez, A. Kurokawa, A. Thissen, A. G. Thomas, A. J. Britton, A. Bernasik, A. Fuchs, A. P. Baddorf, B. Bock, B. Theilacker, B. Cheng, D. G. Castner, D. J. Morgan, D. Valley, E. A. Willneff, E. F. Smith, E. Nolot, F. Xie, G. Zorn, G. C. Smith, H. Yasufuku, J. L. Fenton, J. Chen, J. D. P. Counsell, J. Radnik, K. J. Gaskell, K. Artyushkova, L. Yang, L. Zhang, M. Eguchi, M. Walker, M. Hajdyla, M. M. Marzec, M. R. Linford, N. Kubota, O. Cortazar-Martinez, P. Dietrich, R. Satoh, S. L. M. Schroeder, T. G. Avval, T. Nagatomi, V. Fernandez, W. Lake, Y. Azuma, Y. Yoshikawa, A. G. Shard, Versailles project on advanced materials and standards interlaboratory study on intensity calibration for x-ray photoelectron spectroscopy instruments using low-density polyethylene, J. Vac. Sci. Technol., A 38 (2020) 063208.
[64] S. Tougaard, B. Jørgensen, Absolute background determination in XPS, Surf. Interface Anal. 7 (1985) 17–21.
[65] N. Pauly, F. Yubero, S. Tougaard, Quantitative analysis of satellite structures in XPS spectra of gold and silver, Appl. Surf. Sci. 383 (2016) 317–323.
[66] H. Niehus, W. Heiland, E. Taglauer, Low-energy ion scattering at surfaces, Surf. Sci. Rep. 17 (1993) 213–303.
[67] J. F. Moulder, W. F. Stickle, P. E. Sobol, K. D. Bomben, Handbook of X-ray photoelectron spectroscopy, Physical Electronics, Perkin Elmer., Eden Prairie, Minnesota, USA, 1995.
[68] A. C. Thompson, J. Kirz, D. T. Attwood, E. M. Gullikson, M. R. Howells, J. B. Kortright, Y. Liu, A. L. Robinson, J. H. Underwood, K. J. Kim, I. Lindau, G. P. Williams, J. H. Scofield, X-ray data booklet, Lawrence Berkeley National Laboratory, 2009.
[69] C. Zborowski, T. Conard, A. Vanleenhove, I. Hoflijk, I. Vaesen, Reference survey spectra of elemental solid measured with Cr Kα photons as a tool for Quases analysis (3): Transition metals period 6 elements (Hf, Ta, W, Re, Ir, Pt, Au), Surf. Sci. Spectra 29 (2022) 024004.
[70] L. Sabbatucci, F. Salvat, Theory and calculation of the atomic photoeffect, Radiat. Phys. Chem. 121 (2016) 122–140.
[71] C. Kalha, N. K. Fernando, A. Regoutz, Digitisation of Scofield photoionisation cross section tabulated data, https://doi.org/10.6084/m9.figshare.12967079.v1 (2020).
[72] C. Kalha, N. K. Fernando, A. Regoutz, Digitisation of Scofield Hartree-Fock normalizations and binding energies tabulated data, https://doi.org/10.6084/m9.figshare.13057904.v1 (2020).
[73] C. Kalha, N. K. Fernando, C. Vigil Hernandez, E. E. .Kurtulus, J. Li, Y. Zhou, A. Regoutz, Digitisation of Yeh and Lindau photoionisation cross section tabulated data, https://doi.org/10.6084/m9.figshare.12389750.v2 (2020).
[74] J. Willis, C. Kalha, M. B. Trzhaskovskaya, V. G. Yarzhemsky, D. O. Scanlon, A. Regoutz, Digitisation of Trzhaskovskaya Dirac-Fock photoionisation parameters for HAXPES applications, https://doi.org/10.6084/m9.figshare.13292144.v1 (2020).
[75] J. Willis, C. Kalha, M. B. Trzhaskovskaya, V. G. Yarzhemsky, D. O. Scanlon, A. Regoutz, Digitisation of Trzhaskovskaya Dirac-Fock photoionisation parameters for HAXPES applications, Part II, https://doi.org/10.6084/m9.figshare.13292174.v1 (2020).
[76] M. B. Trzhaskovskaya, V. K. Nikulin, V. I. Nefedov, V. G. Yarzhemsky, Non-dipole second order parameters of the photoelectron angular distribution for elements $z = 1 - 100$ in the photoelectron energy range 1-10 keV, Atom. Data Nucl. Data 92 (2006) 245–304.
[77] V. G. Yarzhemsky, M. B. Trzhaskovskaya, Spectroscopic factors of atomic subshells for HAXPES applications, Atom. Data Nucl. Data 139 (2021) 101387.
[78] S. Tanuma, C. J. Powell, D. R. Penn, Calculations of electron inelastic mean free paths (IMFPS). IV. Evaluation of calculated IMFPs and of the predictive IMFP formula TPP-2 for electron energies between 50 and 2000 eV, Surf. Interface Anal. 20 (1993) 77–89.
[79] S. Tanuma, C. J. Powell, D. R. Penn, Calculations of electron inelastic mean free paths (IMFPs) VI. Analysis of the Gries inelastic scattering model and predictive IMFP equation, Surf. Interface Anal. 25 (1997) 25–35.
[80] H. Shinotsuka, S. Tanuma, C. J. Powell, D. R. Penn, Calculations of electron inelastic mean free paths. X. Data for 41 elemental solids over the 50 eV to 200 keV range with the relativistic full Penn algorithm, Surf. Interface Anal. 47 (2015) 871–888.
[81] W. H. Gries, A universal predictive equation for the inelastic mean free path lengths of x-ray photoelectrons and auger electrons, Surf. Interface Anal. 24 (1996) 38–50.
[82] M. P. Seah, An accurate and simple universal curve for the

energy-dependent electron inelastic mean free path, Surf. Interface Anal. 44 (2012) 497–503.
[83] X. Liu, Z. Hou, D. Lu, B. Da, H. Yoshikawa, S. Tanuma, Y. Sun, Z. Ding, Unveiling the principle descriptor for predicting the electron inelastic mean free path based on a machine learning framework, Sci. Technol. Adv. Mat. 20 (2019) 1090–1102.
[84] A. Jablonski, Universal quantification of elastic scattering effects in AES and XPS, Surf. Sci. 364 (1996) 380–395.
[85] A. Jablonski, C. J. Powell, Improved algorithm for calculating transport cross sections of electrons with energies from 50 eV to 30 keV, Phys. Rev. B 76 (2007) 085123.
[86] A. Jablonski, Photoelectron transport in the surface region of solids: universal analytical formalism for quantitative applications of electron spectroscopies, J. Phys. D: Appl. Phys. 48 (2015) 075301.
[87] J. A. D. Matthew, A. R. Jackson, M. M. El-Gomati, Systematic trends in the transport mean free path with electron energy and atomic number, J. Electron Spectrosc. 85 (1997) 205–219.
[88] I. S. Tilinin, W. S. M. Wener, Escape probability of Auger electrons from noncrystalline solids: Exact solution in the transport approximation, Phys. Rev. B 46 (1992) 13739–13746.
[89] A. Jablonski, C. J. Powell, Information depth and the mean escape depth in Auger electron spectroscopy and x-ray photoelectron spectroscopy, J. Vac. Sci. Technol., A 21 (2003) 274–283.
[90] A. Jablonski, Emission depth distribution function for photoelectrons emitted by laboratory hard X-ray radiation sources, J. Electron Spectrosc. 195 (2014) 26–42.
[91] A. Jablonski, C. J. Powell, Effective attenuation lengths for photoelectrons emitted by high-energy laboratory X-ray sources, J. Electron Spectrosc. 199 (2015) 27–37.
[92] A. Jablonski, The Chandrasekhar function revisited, Comput. Phys. Commun. 196 (2015) 416 – 428.
[93] D. M. Davidović, J. Vukanić, D. Arsenović, Two new analytic approximations of the Chandrasekhar's H function for isotropic scattering, Icarus 194 (2008) 389–397.
[94] S. S. Kawabata, K.and Limaye, Rational approximation formula for Chandrasekhar's H-function for isotropic scattering, Astrophys. Space Sci. 332 (2011) 365–371.
[95] K. Kawabata, S. S. Limaye, Erratum to: Rational approximation formula for Chandrasekhar's H-function for isotropic scattering, Astrophys. Space Sci. 348 (2013) 601–601.
[96] A. Jablonski, S. Tougaard, Escape probability of electrons from solids. influence of elastic electron scattering, Surf. Sci. 432 (1999) 211–227.
[97] N. Pauly, S. Tougaard, F. Yubero, Theoretical determination of the surface excitation parameter from X-ray photoelectron spectroscopy, Surf. Interface Anal. 38 (2006) 672–675.
[98] N. Pauly, S. Tougaard, Determination of the surface excitation parameter for oxides: TiO_2, SiO_2, ZrO_2 and Al_2O_3, Surf. Sci. 602 (2008) 1974–1978.
[99] A. Jablonski, Analytical formalism for calculations of parameters needed for quantitative analysis by x-ray photoelectron spectroscopy, Comput. Phys. Commun. 272 (2022) 108233.
[100] C. S. Fadley, R. J. Baird, W. Siekhaus, T. Novakov, S. A. L. Bergström, Surface analysis and angular distributions in X-ray photoelectron spectroscopy, J. Electron Spectrosc. Relat. Phenom. 4 (1974) 93–137.
[101] C. R. Brundle, B. V. Crist, X-ray photoelectron spectroscopy: A perspective on quantitation accuracy for composition analysis of homogeneous materials, J. Vac. Sci. Technol., A 38 (2020) 041001.
[102] A. Jablonski, Evaluation of procedures for overlayer thickness determination from XPS intensities, Surf. Sci. 688 (2019) 14–24.
[103] P. J. Cumpson, Angle-resolved XPS and AES: Depth-resolution limits and a general comparison of properties of depth-profile reconstruction methods, J. Electron Spectrosc. 73 (1995) 25–52.
[104] R. W. Paynter, M. Rondeau, Comparison of regularization methods for the inversion of ARXPS data, J. Electron Spectrosc. 184 (2011) 43–51.
[105] T. S. Lassen, S. Tougaard, QUASES-ARXPS Software, http://www.quases.com/products/quases-tougaard/.
[106] T. S. Lassen, S. Tougaard, A. Jablonski, Practical correction procedures for elastic electron scattering effects in ARXPS, Surf. Sci. 481 (2001) 150–162.
[107] A. Jablonski, S. Tougaard, Evaluation of validity of the depth-dependent correction formula (CF) for elastic electron scattering effects in AES and XPS, Surf. Interface Anal. 26 (1998) 374–384.
[108] A. Jablonski, S. Tougaard, Practical correction formula for elastic electron scattering effects in attenuation of Auger electrons and photoelectrons, Surf. Interface Anal. 26 (1998) 17–29.
[109] V. I. Nefedov, I. S. Fedorova, Account of photoelectron elastic determination of overlayer thickness, in-depth profiling, escape depth, attenuation coefficients and intensities in surface systems, J. Electron Spectrosc. 85 (1997) 221–248.
[110] Z. Dai, N. Alyabyeva, P. Borghetti, S. Chenot, P. David, A. Koltsov, G. Renaud, J. Jupille, G. Cabailh, R. Lazzari, Al-rich $Fe_{0.85}Al_{0.15}$(100), (110) and (111) surface structures, Appl. Surf. Sci. 509 (2020) 145312.
[111] N. Alyabyeva, S. Chenot, P. David, G. Cabailh, A. Koltsov, J. Jupille, R. Lazzari, Competitive formation of ultra-thin alumina films at the $Fe_{0.85}Al_{0.15}$(110) surface, J. Phys. Chem. C 126 (2022) 19549–19558. doi:https://doi.org/10.1021/acs.jpcc.2c06392.
[112] Z. Dai, P. Borghetti, S. Chenot, P. David, J. Jupille, G. Cabailh, J. Goniakowski, R. Lazzari, Aluminium segregation profiles in the (110), (100) and (111) surface regions of the $Fe_{0.85}Al_{0.15}$ random body-centered cubic alloy, Appl. Surf. Sci. 492 (2019) 886–895.
[113] Z. Dai, N. Alyabyeva, M. Van den Bossche, P. Borghetti, S. Chenot, P. David, A. Koltsov, G. Renaud, J. Jupille, G. Cabailh, C. Noguera, J. Goniakowski, R. Lazzari, Oxide at the Al-rich $Fe_{0.85}Al_{0.15}$(110) surface, Phys. Rev. Materials 4 (2020) 074409.
[114] S. Tougaard, H. S. Hansen, Non-destructive depth profiling through quantitative analysis of surface electron spectra, Surf. Interface Anal. 14 (1989) 730–738.
[115] H. S. Hansen, S. Tougaard, Separation of spectral components and depth profiling through inelastic background analysis of XPS spectra with overlapping peaks, Surf. Interface Anal. 17 (1991) 593–607.
[116] T. R. Bure, O. Renault, E. Nolot, T. Lardin, C. Robert-Goumet, N. Pauly, Assessing advanced methods in xps and haxpes for determining the thicknesses of high-k oxide materials: From ultra-thin layers to deeply buried interfaces, Appl. Surf. Sci. 609 (2023) 155317.
[117] S. Tougaard, QUASES-TOUGAARD Software, http://www.quases.com/products/quases-tougaard/.
[118] R. Zapata, M. Balestrieri, I. Gozhyk, H. Montigaud, R. Lazzari, On the O_2 "surfactant" effect during Ag/SiO_2 magnetron sputtering deposition: the point of view of *in situ* and real-time measurements, ACS Appl. Mater. Interfaces 15 (2023) 36951–36965.
[119] P. S. Bagus, E. S. Ilton, C. J. Nelin, The interpretation of XPS spectra: Insights into materials properties, Surf. Sci. Rep. 68 (2013) 273–304.
[120] R. Hesse, M. Weiß, R. Szargan, P. Streubel, R. Denecke, Comparative study of the modelling of the spectral background of photoelectron spectra with the Shirley and improved Tougaard methods, J. Electron Spectrosc. 186 (2013) 44–53.
[121] S. Doniach, M. Sunjic, Many-electron singularity in X-ray photoemission and X-ray line spectra from metals, Journal of Physics Part C : Solid State Physics 3 (1970) 285–291.
[122] G. D. Mahan, Collective excitations in X-ray spectra of metals, Phys. Rev. B 11 (1975) 4814–4824.
[123] P. Van der Straten, R. Morgenstern, A. Niehaus, Angu-

lar dependent post-collision interaction in Auger processes, Zeitschrift für Physik D Atoms, Molecules and Clusters 8 (1) (1988) 35–45.

[124] M. Schmid, H.-P. Steinrück, J. M. Gottfried, A new asymmetric Pseudo-Voigt function for more efficient fitting of XPS lines, Surf. Interface Anal. 46 (8) (2014) 505–511.

[125] E. Chernysheva, W. Srour, B. Philippe, B. Baris, S. Chenot, R. F. Duarte, M. Gorgoi, H. Cruguel, H. Rensmo, H. Montigaud, J. Jupille, G. Cabailh, S. Grachev, R. Lazzari, Band alignment at Ag/ZnO(0001) interfaces: a combined soft and hard x-ray photoemission study, Phys. Rev. B 97 (2018) 235430.

[126] J. W. Gadzuk, M. Sunjic, Excitation energy dependence of core-level x-ray-photoemission-spectra line shapes in metals, Phys. Rev. B 12 (1975) 524–530.

[127] M. Messaykeh, S. Chenot, P. David, G. Cabailh, J. Jupille, A. Koltsov, P. Lagarde, N. Trcera, R. Lazzari, Core level shifts as indicators of Cr chemistry on hydroxylated α-Al_2O_3(0001): a combined photoemission and first-principles study, Phys. Chem. Chem. Phys. 23 (2021) 21852–21862.

[128] P. Borghetti, E. Meriggio, G. Rousse, G. Cabailh, R. Lazzari, J. Jupille, Photoemission fingerprints for structural identification of titanium dioxide surfaces, J. Phys. Chem. Lett. 7 (2016) 3223–3228.

[129] P. S. Bagus, C. J. Nelin, C. R. Brundle, S. A. Chambers, A new mechanism for XPS line broadening: The 2p-XPS of Ti(iv), The Journal of Physical Chemistry C 123 (2019) 7705–7716.

[130] G. G. Fuentes, E. Elizalde, F. Yubero, J. M. Sanz, Electron inelastic mean free path for Ti, TiC, TiN and TiO_2 as determined by quantitative reflection electron energy-loss spectroscopy, Surf. Interface Anal. 33 (2002) 230–237.

[131] A. H. Al-Bayati, K. G. Orrman-Rossiter, J. A. van den Berg, D. G. Armour, Composition and structure of the native Si oxide by high depth resolution medium energy ion scattering, Surf. Sci. 241 (1991) 91–102.